LAB-SCALE METHODS FOR CARBON COATING ONTO POWDERS AND APPLICATIONS FOR LI-ION BATTERIES

by

Jun Wang

Submitted in partial fulfilment of the requirements

for the degree of Master of Science

at

Dalhousie University

Halifax, Nova Scotia

August 2022

TABLE OF CONTENTS

LIST OF TABLES

LIST OF FIGURES

ABSTRACT

Carbon coating onto fine powders is a commonly used surface modification method in the field of materials science. This is an especially important method for Li-ion battery active materials, which are often carbon coated to improve electrical conductivity and to inhibit surface reactions with electrolyte. In this thesis, two methods of carbon coating technologies were applied on various materials. A new laboratory chemical vapor deposition (CVD) reactor is described, which features an opposing screw rotating fluidized bed. The reactor efficiently concentrates powdered reactants in the reaction zone while maintaining fluidization independent of powder properties. Hydrothermally deposited carbon coatings for Li-ion battery materials were also evaluated. The applied coatings were found to be highly uniform but porous. Nevertheless, carbon coatings on graphite particles produced by both CVD and hydrothermal methods were effective at reducing surface reactions and increasing coulombic efficiency during cycling in lithium cells.

LIST OF ABBREVIATIONS AND SYMBOLS USED

BSE	Backscattered Electrons
C	C as in C-rate
CCCV	Constant Current, Constant Voltage
CE	Coulombic Efficiency
d	Atomic Plane Spacing
DEC	Diethyl Carbonate
EC	Ethylene Carbonate
EDS	Energy Dispersive Spectrometry
FEC	Fluoroethylene Carbonate
FWHM	Full Width at Half Maximum
GICs	Graphite Intercalation Compounds
h	Hours
I	Intensity
LiPAA	Lithium Polyacrylate Acid
n-Si	Nano Silicon
λ	Wavelength of Radiation
θ	Scattering Angle in XRD
ρ	Density

ACKNOWLEDGEMENTS

First and most importantly, I would like to thank my supervisor, Dr. Mark Obrovac, for his great effort to help and guide me, for his continued support, especially during the two years of pandemic. With him, the “impossible mission” for me became an enjoyable and learning process.

I would like to thank my committee, Dr. Robert White, he is always nice to me, encourage me, and give me valuable advice. And I would like to thank my examining committee, Dr. Peng Zhang, too, for his support and valuable time.

I would also like to thank Dr. Tim Hatchard for support and training with all equipment within our lab and all numbers of our group.

Thank Novonix and NSERC for funding.

CHAPTER 1 INTRODUCTION

1.1 Electrochemical Cell Chemistry

In common usage, the term electric battery refers to a device that converts chemical energy into electrical energy. In this thesis, the formal definitions of battery and electrochemical cells will be used, where an electrochemical cell comprises two electrodes (positive and negative) which are immersed in electrolyte solution and a battery comprises two or more electrochemical cells electrically connected. In use, electric current flows from the positive electrode of an electrochemical cell, through an external circuit, to a device to provide energy, and then flows to the negative electrode, to maintain charge neutrality of the entire cell. The main performance parameters of an electrochemical cell are average discharge potential, capacity, internal resistance, and energy density. Cell capacity represents how much charge can pass through the cell during discharge, expressed in units of Ah or mAh. The internal resistance of an electrochemical cell is the resistance to the flow of current through the interior of the cell when it is in operation and is expressed in ohms. Energy density is the electrical energy stored per cell volume or weight. For the same energy requirement, a cell with high energy density can be smaller in size and lighter in weight.

Electrochemical cells are divided into non-rechargeable and rechargeable cells. Non-rechargeable cells are also called primary cells. In primary cells, chemical energy is converted into electrical energy by spontaneous oxidation and reduction reactions within the cell. Primary cells cannot be used after complete discharge because their electrochemical reaction is irreversible. Primary cells, such as the commonly used alkaline cells, are generally cheaper in price and production cost than rechargeable cells.

However, if the cost is calculated over the overall cell life, primary cells are not as economical as rechargeable cells.

Rechargeable cells, also called secondary cells or accumulators, can be recharged after discharge to regenerate their original state. Rechargeable cells are usually more expensive than disposable cells at first, but the total cost and environmental impact is much lower over the cell lifetime. Rechargeable cells are commonly available in lead-acid, nickel-metal hydride, and lithium-ion chemistries. Among all rechargeable cells, lithium-ion cells are utilized in a large number of different applications because of their advantages: high voltage, high capacity, no memory effect, high energy density, low internal resistance, low self-discharge rate, and high cycle numbers. Because of these characteristics, lithium-ion cells have found application in electric vehicles, grid storage, cell phones, notebook computers, video cameras, and many other civil and military applications. On October 9, 2019, the Royal Swedish Academy of Sciences announced that it has awarded the 2019 Nobel Prize in Chemistry to John Goodenough, Stanley Whittingham, and Akira Yoshino for their contributions to the development of lithium-ion cells. This proves how important lithium-ion cells are to our world. Lithium-ion cells continue to be in rapid development. They currently represent the best in modern high-performance cell technology.

1.2 Lithium-ion Cell Chemistry

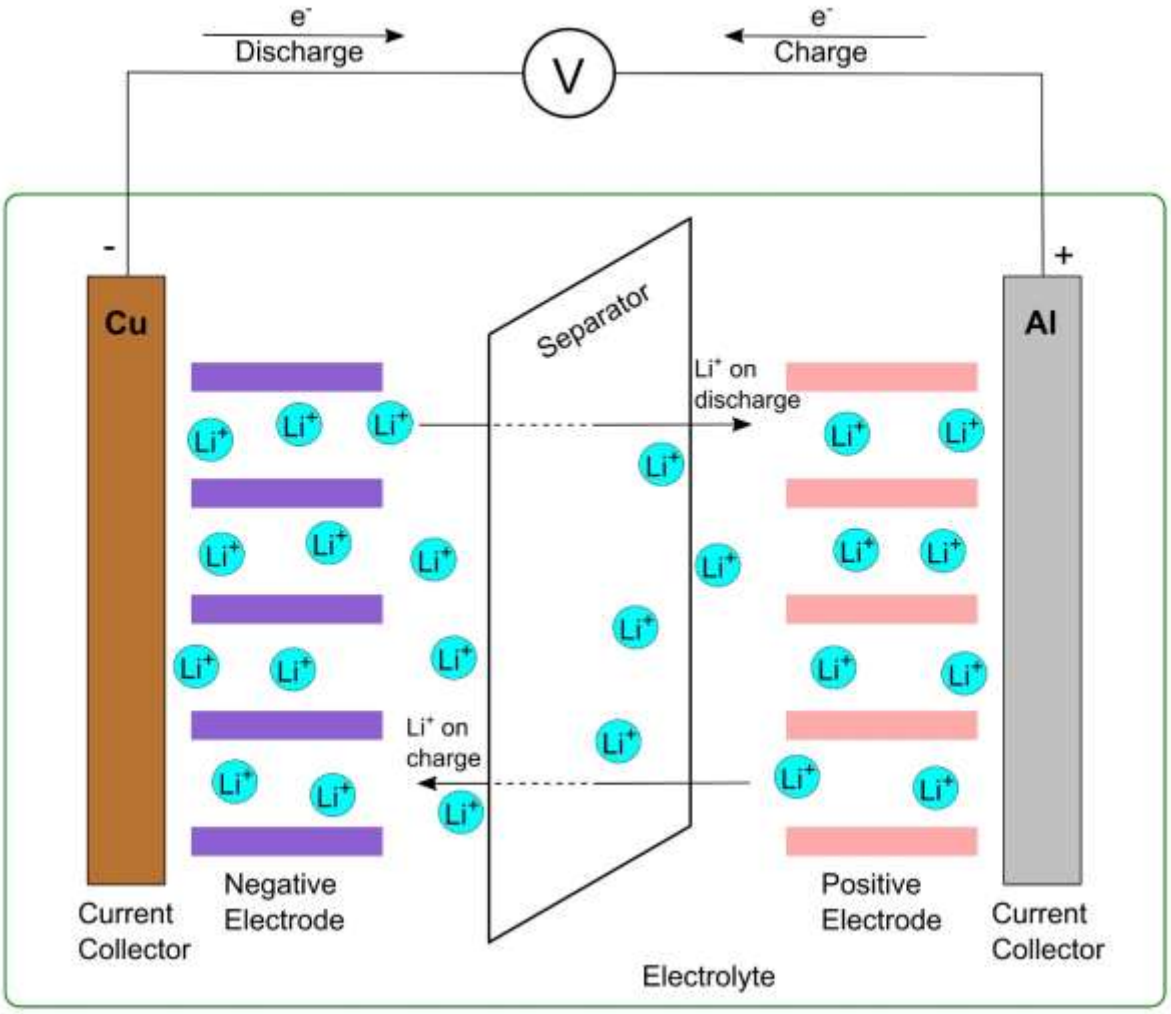

Figure 1.1 Schematic diagram of a lithium-ion battery

A diagram showing the components of a typical lithium-ion cell is shown in Figure 1.1. Lithium-ion cells comprise a positive electrode, a negative electrode, an electrolyte, and a separator. The electrolyte consists of a lithium salt dissolved in an organic solvent, which is the medium through which the lithium ions move between the

positive and negative electrodes. $LiPF_6$ is the most commonly used electrolyte salt. It combines the advantages of stability with the negative and positive electrode, high thermal stability, relatively low cost and toxicity, and high ionic conductivity. Commonly used lithium-ion battery electrolyte solvents are ethylene carbonate (EC), diethyl carbonate (DEC), dimethyl carbonate (DMC), and methyl ethyl carbonate (EMC). The organic solvent quality must be strictly controlled before use, such as the requirements that the purity is above 99.9% and that the moisture content be below 50 ppm (since the water causes decomposition of $LiPF_6$ and can lead to gas generation).

The separator in a lithium-ion cell electrically isolates the positive and negative electrodes, while allowing electrolyte to percolate through its structure, thus providing a path for ion conduction. At present, commonly used separators are composed of multilayers of semi-crystalline polyethylene (PE) and polypropylene (PP). In such polymer films non-tortuous pores can be formed simply by stretching the film. Moreover, when heated (e.g. during a thermal excursion of a battery) the pores close, stopping any electrochemical reactions.

As shown in Figure 1.1, during lithium-ion cell discharge, lithium ions are deintercalated from the anode material, travel through the electrolyte and pass through the separator, and then are inserted into the cathode material at the positive electrode. This process releases an equal number of electrons at the negative electrode. These electrons then flow through an external wire from the negative electrode to the positive electrode, providing electric current which can do work. During lithium-ion cell charge, lithium ions travel from the positive electrode to the negative electrode, and electrons are

forced to flow from the positive electrode to negative electrode by an external power supply.

The more lithium ions that the cathode and anode materials can accommodate, the higher the cell capacity. The greater the potential difference between the positive and negative electrodes, the greater the open circuit voltage of the cell, and the greater the stored energy for a given cell capacity. Therefore, to maximize energy density, positive and negative electrodes are chosen with the highest capacity and highest potential difference.

At present, the most common positive electrode materials in commercial use are lithium cobalt oxide (LCO), lithium iron phosphate (LFP), lithium nickel manganese cobalt oxide (NMC), and lithium nickel aluminum cobalt oxide (NAC).[1,2] Lithium cobalt oxide (LCO) is normally used for small cells due to its higher cost. Lithium iron phosphate (LFP) has relatively low energy density, however its low cost and outstanding safety makes it a popular battery choice for many electric vehicles. Cathode materials containing a ternary mixture of metals (eg: NMC, NAC) have a structure that is very similar to the lithium cobalt oxide structure. Different configurations of NiMnCo elements will bring different performance:

- increasing nickel content increases capacity, but results in reduced cycle performance
- the presence of cobalt can improve material structure, resulting in improved cycling, but too high a Co content will reduce capacity and increase cost

- the presence of manganese can reduce the cost and improve safety, but too high a Mn content can destroy the layered structure of the material and reduce capacity

Therefore, finding the ratio of Ni, Mn, and Co to optimize overall performance is a focus of research and development of NMC materials. A similar optimization is required for NAC materials, where Al replaces Mn to improve structural stability.

At present, graphite is the most widely used Lithium-ion cell anode material. More details about graphite anode materials and their advantages are discussed below. Although silicon has the highest theoretical specific energy density (4008 mAh/g for $Li_{21}Si_5$) of lithium negative electrode materials, there are not many commercial cells that use Si in its pure form because of its huge volume change during lithium insertion and extraction will make it lose its structure and result mechanical failure of the cell.[3,4] To overcome this issue, combining silicon with other elements to form silicon alloy can be effective. The inactive component acts as a matrix material to dilute the volume changes of silicon.[4,5] Lithium titanium oxide (LTO) is another commonly used negative electrode material due to its advantages, like zero-strain property, no lithium plating during quick charging, and good thermal stability in high-temperature conditions.[6] However, the cost of LTO is high considering its lower energy density. Lithium metal has also been considered as a negative electrode material. Lithium has the lowest standard electrode potential (-3.04 V, vs. SHE) and very high theoretical specific capacity (3860 mAh/g). However, it tends to produce lithium dendrites during charging and discharging, which reduces cell efficiency and is also a serious safety hazard. Therefore, lithium metal negative electrodes have not been much used in practice.

1.3 Graphite Anodes

Negative electrode materials for lithium-ion cells need to meet the following requirements.[7]

1. low potential to ensure a high cell voltage.
2. high specific capacity.
3. long cycle life.
4. high electronic conductivity
5. high ionic conductivity
6. low charge transfer resistance
7. can form a stable SEI with the liquid electrolyte.
8. environmentally friendly: no serious pollution to the environment during the production and actual use of the material.
9. low cost/made using abundant resources

It is hard to find a perfect anode material meet all the requirements above. However, graphite has excellent attributes in all of the above categories, including a low lithium potential (0.01-0.2 V), high theoretical specific capacity (375 mAh/g), low cost, and environmental friendliness. Graphite, is a intercalation-based negative electrode material. Its surface area has a great impact on its coulombic efficiency (CE), especially for the first cycle. Graphite with lower surface area generally has higher CE during its formation cycle since less lithium ions will be involved in irreversible reactions with electrolyte on the graphite surface.[8] Graphite's crystallinity affects its capacity a lot. The number of sites in graphite which host lithium ions depends on graphite's crystallinity: greater

crystallinity will result less turbostratic disorder, increasing the capacity. High crystallinity graphite also has good conductivity compared to disordered carbon.[8,9]

When lithium ions are inserted into graphite, graphite intercalation compounds (GICs) form. Dependent on how many lithium ions are intercalated, GICs can be classified into 4 stages (I, II, III, IV). Here, the stage number, n, indicates that every n^{th} interlayer in graphite is lithiated, while the other interlayers are empty. Stage I is the fully lithiated state of LiC_6, in which each graphene interlayer is intercalated. Stage II is a half fully lithiated state, corresponding to LiC_{12}, stage III is LiC_{18}, in which lithium inserted into every three graphene layers, and stage IV corresponds to LiC_{24}. This phenomenon is due to the competition between intra-plane repulsive interactions and in-plane long-range attractive interactions among the lithium ions.[10] The main staged phases of graphite coexist 2-phase regions. Therefore, stages more suitably describe microscopic domains within graphite particles, compared to a whole electrode, since a partially intercalated polycrystalline graphite particle could consist of many small domains that are not necessarily in the same lithiated state. Staging transitions occur from one small domain to another during lithiation.

Lithium intercalation of an electrode is a process of series of stage formation. In general, during lithium intercalation, the very first stage to form is a dilute stage I, followed by a first-order phase transition to stage IV.[11] Then, stage III, stage II, and finally stage I, a fully lithiated state, are formed. When deintercalation happens, the order of stage occurrence is reversed.

In a lithium-ion cell with graphite as negative electrode, a solid-electrolyte-interphase (SEI) will form during the first lithiation process. The SEI is ionically

conductive but electronically insulating. The thus formed SEI acts like a protective layer to impede continuous electrolyte decomposition.[8] The graphite surface is classified as basal and edge planes in the aspect of the structure of carbons.[12] The SEI layer mostly forms at the edge plane and defect sites, since the lithium ions can only intercalate through the non-basal planes. The SEI layer growth in lithium-ion batteries is commonly assumed to have a $t^{\wedge 0.5}$ (t = time) dependance based on many experimental measurements.[13]

Graphite may be classified as natural graphite and synthetic (or artificial) graphite, in general. Natural graphite can be further classified into three types, flake graphite, lump graphite, and amorphous graphite.[14,15] For natural graphite, its cost is low considering its specific capacity. However, the cycle life of natural graphite is low compared to most synthetic graphites. The performance of synthetic graphite is more balanced, and normally the compatibility with electrolyte is better. It is economically worthwhile to modify the natural graphite into some form of better graphite for lithium-ion battery use. One method normally used is spheroidizing the natural graphite. By curling the basal edges and classifying the fine natural graphite particles, low surface area and dense spherical natural graphite can be obtained.

To sum up, graphite is the dominate anode material used in lithium-ion cells. However, graphite can have several disadvantages: (1) flake graphite powder has a large specific surface area, which has a large impact on the first charge/discharge efficiency; (2) the layer spacing of graphite is small, which increases the Li^+ diffusion resistance;[16] (3) the flake structure of graphite determines that Li^+ can only be intercalated from the

end face of the material and gradually diffuse into the internal particles, leading to long and uneven Li^+ diffusion paths.[16]

1.4 Carbon Coatings for Graphite

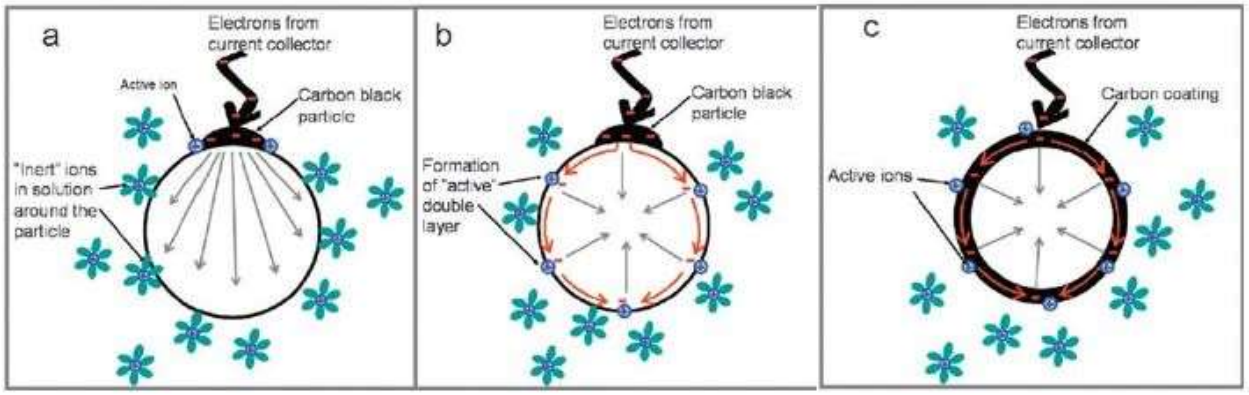

Figure 1.2 Schematic conduction/diffusion of electron and Li ions.[17]

To solve the above inherent drawbacks of graphite, it needs to be modified. An effective modification is to coat graphite particles with an amorphous carbon layer. In a lithium-ion cell, the negative electrode is usually made by adding some carbon black as conductor to the active negative electrode materials to increase the electronic conductivity, as shown in Figure 1.2 (a,b). The carbon black is normally point-contacted with the active material particles. Under these circumstances, if the electronic conductivity of the active particles is worse than its ionic conductivity, then most of active ions from the electrolyte will trend to aggregate where the carbon black contacts the active particle because the active particle lacks the ability to transfer the charge to its other parts (as shown in Figure 1.2 (a)). Conversely, if the electronic conductivity of the active particles is better than its ionic conductivity, there will be formation of a double

layer on the surface of active particles because the active ions don't get enough time to diffuse into the active particles (as shown in Figure 1.2 (b)). Both situations will increase the electrode resistance, which is detrimental for quick charging and discharging. Fortunately, the issue can be solved by coating the active particles with a layer of amorphous carbon, shown in Figure 1.2 (c). The layer of amorphous carbon material covers the graphite surface, which can improve lithium ion diffusion and the electronic conductivity of the active particles, thus improving rate capability. Due to the very good chemical stability of amorphous carbon, the carbon coating will also help to reduce the contact between the active particles and electrolyte. The coated layer can stop the SEI layer growth or at least reduce its rate of formation.

There are two common carbon coating methods: one is to mix graphite with a precursor carbon source material (eg: PVC), and then to heat the mixture material to high temperature (normally 1000°C) to carbonization the coated layer. The main issue of this method is that the product has to be ground and classified, since it tends to form huge lumps instead of individual particles. Another carbon coating method is chemical vapor deposition (CVD), this method is widely used in industry and involves complex and expensive equipment, which is not very practical in research labs.

In this thesis, improved carbon coating methods for lithium-ion active material powders at the laboratory scale were investigated. An innovative laboratory chemical vapor deposition reactor was designed and implemented. It contains a set of opposing screws to maintain a rotating fluidized bed that concentrates samples in the reaction zone. This device has ability to deal with small samples, which is very useful for exploratory research in fields such as battery materials. The density and electrochemical properties of

the coated carbon were evaluated by coating carbon onto inert Al_2O_3 particles. The coatings were also evaluated on graphite particles. In this study, the hydrothermal carbon coating method was also evaluated. Compared to the CVD method, the carbon coating applied by hydrothermal method onto powders were found to be highly porous. However, the hydrothermal carbon coating was also effective at reducing surface reactions and increasing coulombic efficiency during cycling in lithium cells. The carbon coating methods developed in this thesis were also found to be useful in the synthesis of entirely new materials, which is also discussed in this thesis.

CHAPTER 2 EXPERIMENTAL TECHNIQUES

2.1 X-ray Diffraction

X-ray diffraction (XRD) is a commonly used non-destructive characterization technique for crystalline solids. X-rays have a wavelength between 0.01 to 10 nanometers, which is close the scale of the distance between lattice planes in a crystal. Therefore, when incident X-rays strike atoms that are arranged in a series of lattice planes, diffracted X-rays will interfere constructively when the path difference between X-rays is equal to an integer multiple of X-ray wavelengths. The condition for constructive interference can be used to determine crystal structure. In addition, grain size, grain orientation, and lattice strain can also be determined from XRD patterns.

In an XRD instrument, X-rays are commonly generated by a diode vacuum tube, which has a filament electron source and a heavy metal target. The target metal is normally copper, tungsten, or nickel. When a high voltage (e.g. 45 kV) is applied between the electron source and target, electrons are accelerated from the source and towards the target, where they impact and transfer their energy to the target's constituent metal atoms. The inner shell electrons of a target metal atom can be ejected by the incident electron. Subsequently, electrons from the metal atom's outer shell can drop its energy level to fill the resulting vacancy. This process results in the emission of an characteristic X-ray photon, which has energy equal to the difference between the inner shell electron energy level and the ejected outer shell electron energy level. The generated X-rays are emitted in all directions. A series of slits collimates the X-rays into a beam incident to the sample. The diffracted X-rays are collimated to a point and

converted into an electronic signal by a detector. XRD patterns are often plotted as the intensity of the scattered radiation vs. scattering angle.

The constructive interference condition can be described by Bragg's Law:[18]

$$n\lambda = 2d \sin\theta \tag{2.1}$$

Where n is an integer, λ is the incident X-ray wavelength, d is lattice spacing distance, and θ is the angle between incident X-ray and crystal planes.

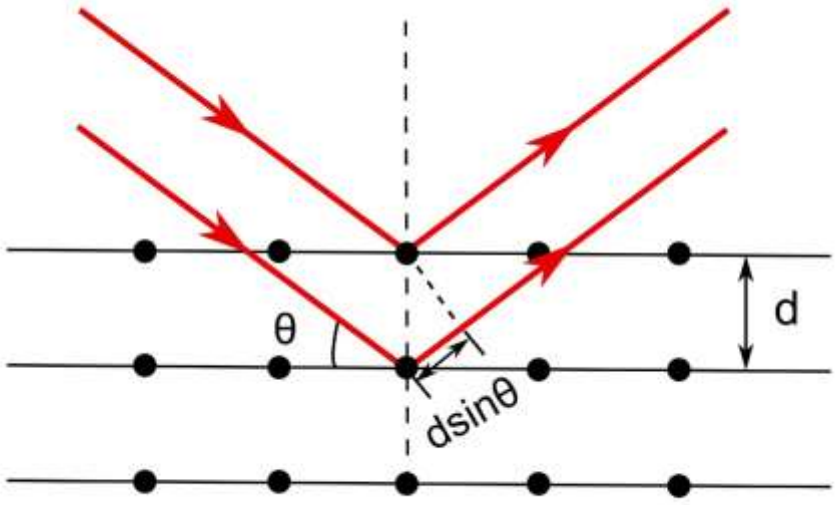

Figure 2.1 Schematic diagram of Bragg diffraction from crystalline planes in a solid.

Figure 2.1 illustrates the Bragg condition for diffraction. X-ray beams with identical wavelength approach a crystalline solid and are scattered by different atom layers of the solid. The lower X-ray traverses an extra length, 2dsin θ. Constructive interference occurs when this length is equal to an integer multiple of the X-ray wavelength.

The average grain size, τ, of crystalline phases can be estimated by the Scherrer equation:[19]

$$\tau = k\lambda/(H \cos \theta) \quad (2.2)$$

Where k is the shape factor (~0.94 for cubic particles), H is the full width at half maximum (FWHM) of a XRD peak measured in Θ units, and λ is the incident X-ray wavelength.

In this thesis, all XRD patterns were collected using a Rigaku Ultima-IV X-ray diffractometer equipped with a copper target, and a scintillation counter detector with a diffracted beam monochromator. The X-ray generator accelerating voltage was 45 kV and the filament current was set at 40 mA. Samples were compressed into a stainless-steel sample well of dimensions 25mm by 20mm by 3mm, such that the top of the sample was flush with the upper surface of the sample holder. Measurements were taken in 0.05° 2θ steps with a count time of 6 seconds per step, in the range of 10° to 80° 2θ.

2.2 Scanning Electron Microscopy and Energy Dispersive X-ray Spectroscopy

A scanning electron microscope (SEM) is a useful tool that utilizes a focused beam of electrons to investigate the surface topology of materials. High energy electrons (e.g. 1000 keV) have very short wavelength (normally less than 1 nm), this enables the observations of objects at a very high resolution.[20] A typical SEM can operate at magnifications that are easily adjusted from 10× to 300000×.

During SEM operation, electrons are produced by a thermionic field in an electron gun and accelerated by an applied potential (0.1~50 keV), so that they travel through one or two focusing condenser lenses. When the high energy electron beam interacts with the specimen, both elastic and inelastic scattering can happen. Elastic

scattering means there is only a change in the direction of the incident electron without almost no energy loss. The deflected backscattered electrons (BSE) normally have nearly the incident beam energy. Heavier atoms scatter more backscattered electrons, resulting in a brighter region in final images. Inelastic scattering occurs when the electron beam interacts with the electrons of the specimen atoms. This results in a transfer of energy to the atom and an ejection of an electron from the atom as a secondary electron (SE). Secondary electrons normally have less energy than the incident electrons. Secondary electrons normally are good for topographic contrast in SEM images, such as surface texture and roughness since they are mostly generated from regions near the surface of a specimen.

If a vacancy (due to the ejection of a secondary electron) is filled by an outer shell electron during the interaction between the incident electron beam and the specimen atoms, a characteristic X-ray will be generated.[7,9] The energy and intensity of the generated X-rays can be measured by detectors, and the spectrum can be analyzed quantitatively. This is called energy-dispersive X-ray spectroscopy (EDS). EDS can be used for quantitative elemental analysis and can be used to generate composition analysis element maps of SEM images.

In this thesis, SEM images and EDS element maps were collected with a TESCAN MIRA 3 field-emission scanning electron microscope. Samples were adhered to a conductive carbon tape. All images were collected at an accelerating potential of 5 kV.

2.3 Ion Milling

An Ion mill is a machine that uses a high energy argon ion beam to ablate material from a specimen. It is used for obtaining sample cross sections. Three main factors can influence the cutting process: time, working potential, and argon flow. The cutting depth is determined by working time and material type; the potential required by the argon gas flow rate, which has to be stable to cut efficiently. Both insufficient and excess gas flow can make the cutting beam unstable. Back sputtering is a common issue of ion milling when the high energy cutting beam is too powerful or is at a bad angle. Ions are directed at the surface of particles, and upon arrival, they can transfer their energy to surface atoms which escape. These escaping atoms can deposit onto the surface of the original material (referred to here as "back sputtering"), providing false atomic distribution information and making the underlying microstructure hard to identify.

In this thesis, a JEOL IB-19530CP Cross Section Polisher (CP) was used to prepare smooth cross-sections of specimens. All samples were cross-sectioned at 6 kV with an argon gas flow of 5.5 (a unitless machine setting).

2.4 Thermogravimetric Analysis

Thermogravimetric analysis (TGA) is a method in which a sample's weight is measured as a function of its temperature. The results can reveal the information about how the specimen reacts in a specific atmosphere (e.g. air, argon or helium) during temperature changes.

In this thesis, all TGA measurements were performed with a NETZSCH TG 209F3 thermogravimetric analyzer with compressed air as purge gas (flow rate: 20 ml/min), in a heating range from 20°C to 800°C with 10°C/min heating rate.

2.5 Raman Spectroscopy

Raman spectroscopy is an important technique to determine the vibrational modes of molecules. Especially, Raman spectroscopy is good at detecting the symmetric vibrations of non-polar groups.[21] This technique involves a two-photon inelastic light-scattering event, while the incident photon has greater energy than the scattered photon. The energy difference between the incident photon and scattered photon is the energy of the molecular vibration. Therefore, the scattered photon will reduce its frequency since the energy of a photon is proportional to its frequency.

The vibrational energy levels of a molecule depend on the masses of its constituent atoms, their geometric arrangement, and the strength of their chemical bonds.[21] Therefore, the vibrational energy levels are unique for each specific type of molecule. Hence, Raman spectra provide a "fingerprint" that includes specific information about a molecule, such as molecular structures, dynamics, and environment.

In practice, specimens are illuminated by a laser beam, then the electromagnetic radiation from the illuminated spot is collected with a detector. The Raman spectrum is the scattered photon intensity as a function of the frequency shifts.

Raman spectroscopy is a useful tool for studying carbon films. Raman spectra of carbon can reflect differences in bonding of different forms of carbon.[22] It can provide characterization information of the carbon films when the disordered carbon peak (D peak) and the graphite peak (G peak) are distinct in the spectrum.[23] Graphite has a Raman band at 1575 cm^{-1}, while the disordered carbon or nanocrystalline graphite shows broadened bands and enhanced intensity around 1355 cm^{-1}.[22,24,25] For amorphous carbon, there is a broad band, peaking from 1500 to 1570 cm^{-1}.[22] In general, certain types of

carbons have their own specific patterns and peaks. By analyzing the spectra, structural information of the carbon sample can be obtained.

In this thesis, the Raman analysis were performed using a HORIBA T64000 Raman spectrophotometer. The excitation laser beam wavelength was 532 nm, dwell time was 10 s, objective lens was 100x, and repetitions was 10x.

2.6 Electrochemical Techniques

Coin-type cells are widely used for testing new materials in Li-ion battery research because the assembly of such cells is easy and quick. Coin cells comprise a positive electrode and a negative electrode separated by a separator drenched in an ion-conductive electrolyte. Half-cells refer to a coin cell configuration in which a working electrode comprising the material of interest are cycled against a lithium metal counter/reference electrode.

In this thesis, half-cells were used for all electrochemical measurements. A typical half-cell stack consisted of a working electrode, two separators (Celgard 2300), a lithium metal electrode (99.9%, 0.38 mm thick, Sigma Aldrich), and two copper spacers (each 0.03 inches thick) in series, as shown in Figure 2.2.

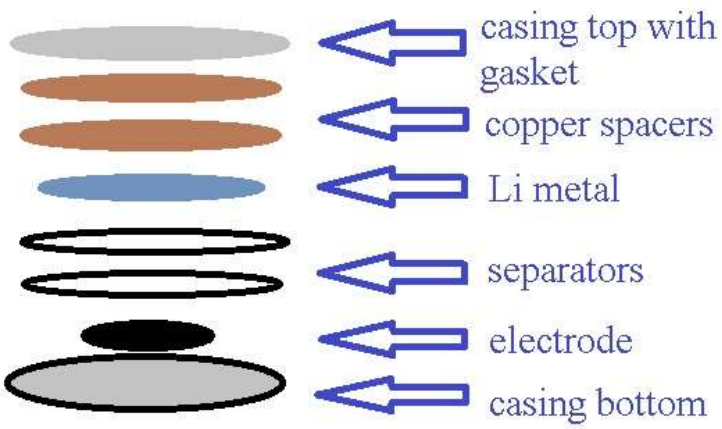

Figure 2.2 Schematic diagram of half coin cells.

To prepare coin cell electrodes, first a slurry containing the active material powder, conductive carbon, and binder was prepared. Different component ratios were used depending on the project. The conductive carbon was carbon black (Super C65, Imerys Graphite and Carbon). Binders used were polyvinylidene fluoride (PVDF, Kynar HSV 900) or lithium polyacrylate (LiPAA) (from a 10 weight% LiPAA aqueous solution, made by neutralizing a polyacrylic acid solution (Sigma-Aldrich, average molecular weight of 250000 g per mol, 35 wt% in water) with $LiOH \cdot H_2O$ (Sigma Aldrich, 98%)). Slurries were mixed using a high-shear mixer equipped with a Cowles-type blade impeller at 5000 rpm for 10 min. and then spread onto electrolytic copper foil (Furukawa Electric, Japan) with a 0.1 mm gap coating bar. The coatings were dried in air at 120 °C for 40 min., punched into 1.3 cm (in diameter) disks, and then heated under vacuum for a few hours at 120 °C with no further air exposure before cell assembly.

The electrolyte used was 1M $LiPF_6$ (battery grade from BASF) dissolved in a solvent mixture of ethylene carbonate (EC), diethyl carbonate (DEC), and fluoroethylene carbonate (FEC) (all battery grade from BASF) in an EC:DEC:FEC volume ratio of 3:6:1. For every cell, 168 μL of electrolyte was used. Separators were soaked in electrolyte before cell assembly.

Most cells were cycled between 0.007 V and 0.9 V at constant current rates. A Neware battery testing system was used to measure the performance of the cells at a C/10 rate for the 1st cycle and a C/5 rate for the following cycles, where C-rate is defined here as the current required to fully discharge an electrode material in one hour according to its theoretical capacity.

CHAPTER 3 LAB-SCALE CHEMICAL VAPOR DEPOSITION ONTO POWDERS

3.1 Introduction

Chemical vapor deposition (CVD) is a well-known coating technique currently in use in manufacturing and in research laboratories. There are many types of CVD methods to coat a variety of material formats. The film deposited can be in the form of metastable phases that are inaccessible by other methods; where phase formation can be carefully controlled, depending on the processing conditions.[26,27] For fine powder particle coating, efficient contact needs to be maintained between the reactive gas and the solid particles to be coated.[28] Normally, a powder CVD apparatus involves a fluidized bed in which the powder is agitated, so as to expose all powder surfaces to the reactive gas flow while maintaining the powder in the reaction zone. During processing, the reaction zone is heated (typically to temperatures above 600 °C for carbon coating) and a reactive gas flow is established (e.g. ethylene, in the case of carbon coating). Any powder that escapes the reaction zone during processing can reduce yield or, even worse, become mixed with the final product, leading to inhomogeneous coating results. Achieving an efficient fluidized bed while confining the particles to the reaction zone can be difficult to achieve, especially at the laboratory scale where samples are small (e.g. <10 g) and the reaction zone might be only a few centimeters in length.

This chapter has previously been published in [Wang, J., & Obrovac, M. N. (2022). Lab-scale chemical vapor deposition onto powders. AIP Advances, 12(7), 075209.], where both authors contributed equally.

There are two main methods of establishing a fluidized bed in a CVD reactor.[28,29] These methods are illustrated in Figure 3.1. One method is by employing a rotary furnace, as shown in Figure 3.1(a). This method relies on the rotation of the furnace tube to establish sample fluidization. Sample residency within the reaction zone is influenced by the rotation speed, gas flow, and by tipping the entire furnace/tube assembly. This method is particularly useful for continuous processing. When operated for batch processing small samples in the lab, the furnace angle, gas flow, and rotation speed need to be adjusted carefully to keep the particles within the reaction zone.

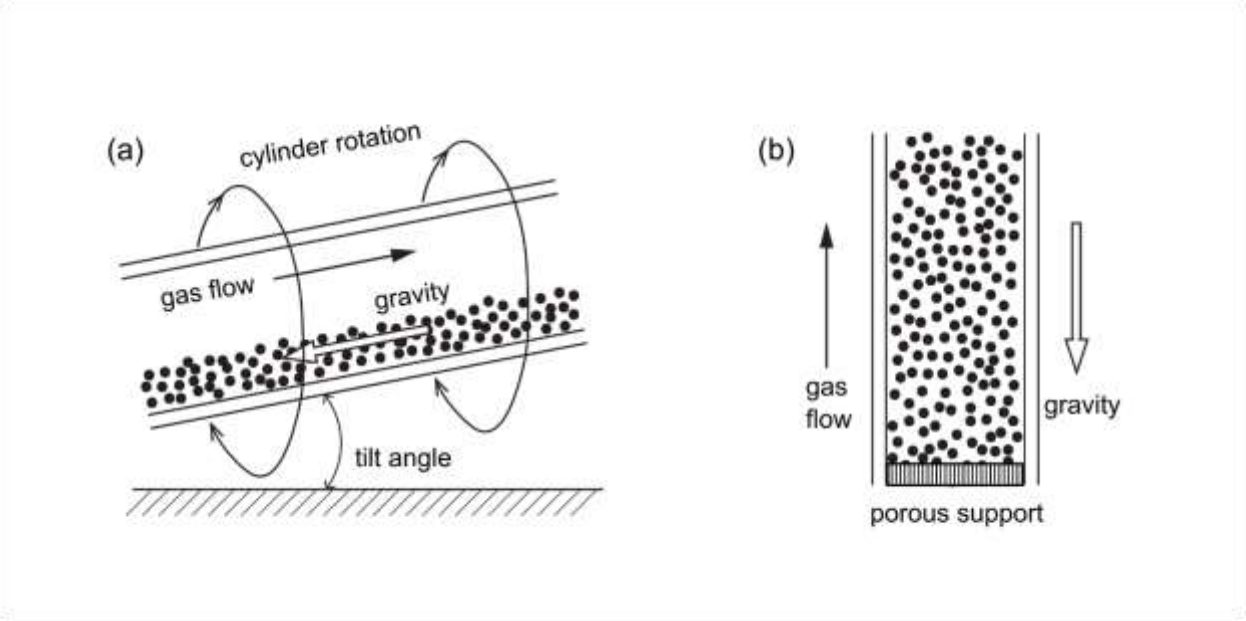

Figure 3.1 Schematic diagram of (a) a rotary CVD furnace and (b) a vertical CVD furnace.

These parameters change for different sample types and can change during CVD processing, as particle characteristics change because of thermal effects (e.g. loss of moisture at the particle surface), electrostatic charge effects or because of changes in

surface properties or aggregation due to the CVD coating. Obtaining a good balance of all these parameters for a new powder sample batch is difficult, and keeping these parameters continuously balanced during the coating process is even more challenging; often leading to low yields and inhomogeneous coating results, especially for small sample sizes.

Vertical reactors, shown in Figure 3.1(b) are also used for applying CVD coatings to powders, especially for small laboratory samples.[28,29] In a vertical reactor, the sample initially sits on a porous plug within the furnace tube. Reactive gas flow is adjusted to establish fluidization. In such reactors, achieving fluidization depends on the reactive gas flow, particle shape, particle density, and particle surface characteristics. Depending on the sample, fluidization may be difficult or impossible to attain or maintain, especially if the sample has a high density or has a tendency to aggregate, resulting in the gas to form channels through the powder sample, rather than uniform fluidization. As with a rotational furnace, establishing optimal parameters for new samples is challenging, as is maintaining fluidization during the CVD process. Both methods have the drawbacks of the fluidization parameters being coupled with powder properties (making it difficult to maintain fluidization as particle properties change during the CVD process) and also being coupled with the reactive gas flow (limiting CVD reaction conditions based on reactive gas flows necessary to maintain fluidization). For the above reasons CVD processing using conventional horizontal rotational reactors or vertical reactors is highly challenging at the laboratory scale, where typically many small batches of materials, each often having different properties, need to be processed.

One application of CVD powder processing is the carbon coating of graphite powders for use as active negative electrode materials in Li-ion batteries. Both artificial and natural graphites are utilized. Despite is lower cycle life, natural graphite is utilized extensively as the negative electrode in Li-ion batteries because of its low cost. However, due to its relatively active edge structure, natural graphite can easily react with electrolyte during Li-ion battery operation. This can cause electrolyte decomposition reaction products to accumulate on the graphite surface, forming an solid electrolyte interphase (SEI). Continual growth of the SEI during cell operation can lead to increased battery internal resistance and lithium consumption. Both these effects can in turn result in capacity loss. Coating both artificial and natural graphites with carbon can reduce surface reactivity, resulting in reduced SEI growth and increased cycle life.[17]

This chapter describes a CVD reactor for laboratory use that utilizes a unique rotating reaction tube that can achieve fluidization of small particle batches, regardless of the powder properties, while efficiently confining the sample to a small reaction zone. To test and apply this lab-made apparatus, an aluminum oxide sample and a graphite sample were carbon coated successfully by using ethylene gas as a carbon source. From these samples, the density and the electrochemical properties in lithium cells of the coated carbon layer were determined. It was found that this reactor system can be used for CVD coating small batches of different powders without the need for any optimization of the fluidized bed, making it ideal for laboratory use.

3.2 Experimental

3.2.1 The CVD Reactor

The CVD reactor utilized in this study was designed to confine small amounts of fluidized powder to the reaction zone of a furnace, irrespective of the powder properties. This was accomplished with a rotating reactor tube having internal fins in an opposing screw configuration. The CVD reactor is shown schematically in Figure 3.2(a). It consists of the following compartments:

1. A rotating quartz tube with inner opposing screws ~90 cm in length with an inner diameter of 25 mm. The opposite spiral structure has a length of 20 cm. During tube rotation, the opposing screws efficiently fluidize the sample powder while simultaneously concentrating the powder in the reaction zone in the middle of the tube. The sample size could be from 0.5 cm^3 to 10 cm^3, regardless its true density or weight.
2. A laboratory tube furnace with a ~25 cm heating zone.
3. An electric motor with a speed controller to drive the tube.
4. Rotation joints with gas feed throughs.
5. Mineral oil bubblers to provide gas seals and keep a constant pressure in the reaction tube.
6. Ar gas source.
7. Ethylene gas source.
8. A gas flow meter.

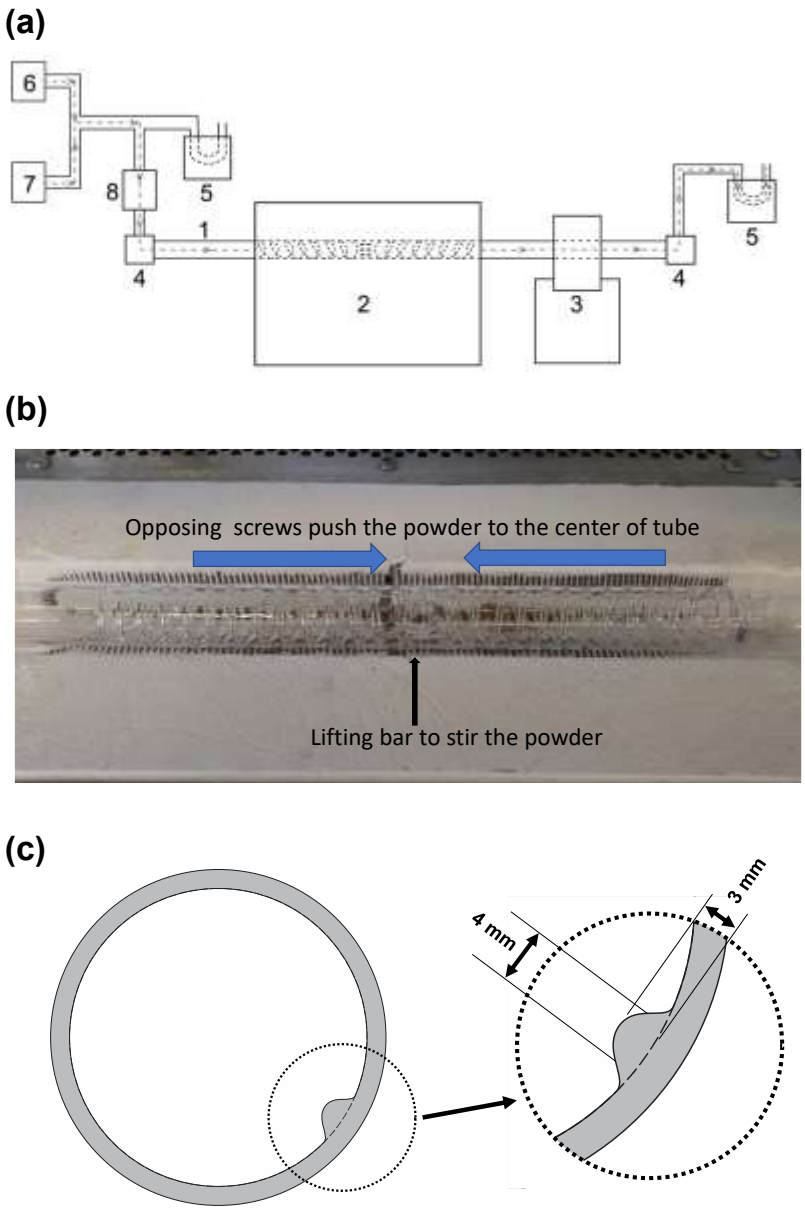

Figure 3.2 (a) A schematic diagram of the opposing screw rotating fluidized bed CVD setup. The opposing screw reactor tube is shown in detail with arrows indicating the direction of powder flow towards the center of the tube (where lifter bars are located) during tube rotation). (b) A photograph of the opposing screw reactor tube centered in the heated zone of a furnace. (c) Cross section of opposing screw reactor tube with an inset showing the profile of a screw fin in detail.

3.2.2 CVD Procedure

5 mL (3 mL based on true density) of Al_2O_3 powder (600 mesh Aluminum Oxide Grit from Kramer Industries Inc.) or graphite powder (MesoCarbon MicroBeads, from China Steel Chemical Co., particle size ~26 microns) was carefully placed at the center of the CVD furnace tube. Glass filter paper was packed into the furnace tube outlet to stop tar from accumulating in the exhaust gas lines. The loaded tube was assembled into the CVD setup, according to Figure 3.2(a) and was purged with Ar gas (60 ml/min.) for 1 hour. While still under Ar-gas flow, tube rotation was started at ~100 rpm and the temperature was increased to 800°C in 30 minutes. The Ar gas flow was then stopped, and a flow of ethylene gas was established through the tube at 80 ml/min. for the desired CVD processing time (eg. 5 hours), while the tube was under constant rotation and heated at 800°C. The flow of ethylene gas was then stopped, Ar was reintroduced in the tube at 60 ml/min., and the furnace was allowed to cool. Rotation was stopped only after the sample reached room temperature. Samples were carefully collected from the furnace tube without contamination from accumulated downstream tar.

3.2.3 Material Characterization

X-ray diffraction (XRD) patterns were measured using a Rigaku Ultima IV powder diffractometer X-ray system equipped with a Cu Kα X-ray source, a diffracted beam monochromator, and a scintillation detector. Each XRD pattern was collected from 10° to 80° 2-theta in 0.05° increments for 3 seconds per step. Laser Raman spectroscopic measurements were performed in the 1200 - 1700 cm^{-1} region with a laser radiation wavelength of 532 nm and a power of 15mW using a HORIBA T64000 Raman spectrophotometer. Sample powder cross sections were prepared with a JEOL Cross-

Polisher (JEOL Ltd., Tokyo, Japan) and sample powder morphologies were studied with a TESCAN MIRA 3 LMU variable pressure Schottky field emission scanning electron microscope (SEM) at 5.0 kV and 20.0 kV. The sample densities were measured with dry helium gas using a Micromeritics AccuPyc II 1340 gas pycnometer. Thermal gravimetric analysis (TGA) was conducted using a NETZSCH TG 209F3 thermogravimetric analyzer with compressed air as purge gas (flow rate: 20 ml/min), in a heating range is from 20°C to 800°C with 10°C/min heating rate. A summary of the coated carbon content, true density, and BET surface area of the samples prepared in this study is provided in Table 3.1.

Table 3.1. Coated carbon content, true density, and BET surface area of the samples prepared in this study.

Sample	Coated Carbon Content (wt %)	True Density (g/cm^3)	Surface Area (m^2/g)
Al_2O_3	0%	3.98	0.39
C-Al_2O_3(5h)	13%	3.46	0.50
graphite	0%	2.18	0.29
C-Gr(1h)	10%	2.14	0.20
C-Gr(2h)	19%	2.10	0.19

3.2.4 Electrochemical Characterization

C-Al_2O_3(5h) electrode slurries were prepared from C-Al_2O_3(5h), carbon black (Super C65, Imerys Graphite and Carbon), and lithium polyacrylate (LiPAA) (from a 10 weight% LiPAA aqueous solution, made by neutralizing a polyacrylic acid solution (Sigma-Aldrich, average molecular weight of 250000 g per mol, 35 wt% in water) with LiOH·H2O (Sigma Aldrich, 98%)) in a volumetric ratio of 70/5/25 (corresponding to a 83/4/13 weight ratio) with a few drops of wetting agent (isopropanol, Sigma-Aldrich, 99.5%) in distilled water. C-Gr electrode slurries were prepared from C-Gr, carbon black, and polyvinylidene fluoride binder (PVDF, Kynar HSV 900) in a mass ratio of 96/2/2 with an appropriate amount of N-methyl-2-pyrrolidone (NMP, Sigma Aldrich, anhydrous 99.5%) to establish a good slurry viscosity. Slurries were mixed using a high-shear mixer equipped with a Cowles blade at 5000 rpm for 10 min. and then spread onto electrolytic copper foil (Furukawa Electric, Japan) with a 0.1 mm gap coating bar. The coatings were dried in air at 120 °C for 40 min., punched into 1.3 cm (in diameter) disks, and then heated under vacuum for a few hours at 120 °C with no further air exposure before cell assembly.

Electrodes were assembled into 2325-type coin cells with a lithium foil (Aldrich, 99.9%) counter/reference electrode separated by two layers of separators (Celgard 2300) in an Argon filled glove box. 168 μL of electrolyte was used in each half cell. The electrolyte consisted of 1M $LiPF_6$ (BASF) in a solution of ethylene carbonate (EC), diethyl carbonate (DEC), and mono-fluoroethylene carbonate (FEC) (volume ratio 3:6:1, all from BASF). Cells were cycled at 30 °C between 7 mV and 0.9 V using a Neware battery testing system at a C/10 rate for the 1st cycle and a C/5 rate for the following

cycles. Cells were held at 7 mV after discharge (lithiation) until a rate decreased to C/20 for the first cycle or C/10 for subsequent cycles, to simulate CCCV charging in a full cell. Electrochemical impedance spectra (EIS) were measured using a Bio-Logic VMP3 potentiostat/EIS spectrometer. EIS measurements were performed at 20 °C with a 10 mV amplitude excitation and a frequency range from 100 kHz to 10 mHz.

3.3 Results and Discussion

The opposing screw reactor tube is shown in detail in Figure 3.2(b). It consists of a quartz tube to which inner fins (also quartz) have been fused to form opposing screws. A cross-section of the tube showing the profile of a screw fin and its approximate dimensions is shown in Figure 3.2(c). When rotated during operation, the screws confine the sample powder to the center of the tube, while fluidizing the powder mixture. An additional quartz lifter bar at the center of the tube enhances fluidization further. This CVD reactor design provides an effective fluidized bed, while simultaneously confining even very small sample amounts within the reaction zone. This is a significant improvement over traditional CVD methods, especially for small sample sizes. Moreover, unlike traditional horizontal rotating tube or vertical tube fluidized beds, no adjustment was needed between particle samples with different morphologies, compositions and densities. This enables rapid CVD processing of many different small samples, which is typically needed for materials development.

Samples carbon coated utilizing the CVD reactor are denoted here using the following notation "C-Al_2O_3(5h)" for carbon coated Al_2O_3 and "C-Gr(2h)" for carbon-coated graphite, where the quantity in brackets is the CVD processing time. Al_2O_3

particles were carbon coated to characterize the nature of the carbon deposited by the reactor. Figure 3.3(a) shows an SEM image of uncoated Al_2O_3. The Al_2O_3 particles are about 9 μm (D10) - 20 (D90) μm in size, with a median (D50) size of 14 μm. The particles are irregularly shaped, with smooth sides and sharp edges. The BET surface area of these particles was measured to be 0.39 m^2/g. Using the measured density of these particles of 3.98 g/ml, this corresponds to a volumetric surface area of 1.55 m^2/ml. After 5h carbon coating (Figure 3.3(b)) the resulting C-Al_2O_3(5h) particles are uniformly covered with a thick carbon layer, excepting a few areas in which the coating has flaked off. It was noticed that carbon coatings can flake off smooth substrates, especially when they become thick (> 0.1 μm). Figure 3.3(c) shows an SEM image of cross-sectioned C-Al_2O_3(5h) particles. Except where flaking has occurred, the particle surfaces are completely coated with a dense carbon layer that is about 0.2 - 0.7 μm in thickness. EDS maps of C, Al, and O (Figure 3.3(d-f), respectively) more clearly show the encapsulation of the Al_2O_3 particles within a pure carbon layer that has little oxygen content.

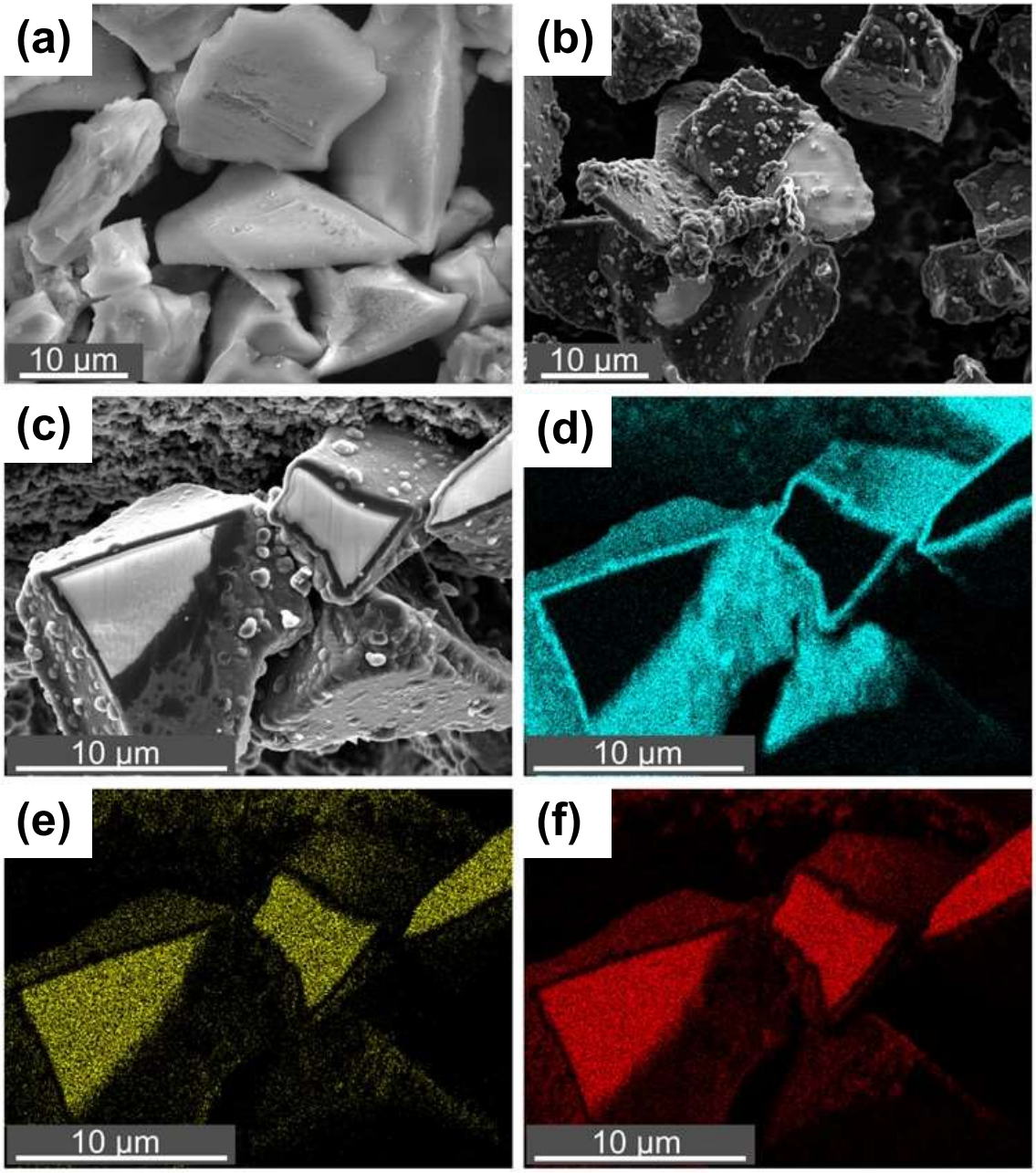

Figure 3.3 SEM images of (a) uncoated Al_2O_3 powder, and (b) C-Al_2O_3(5h). (c-f) SEM images of cross-sectioned C-Al_2O_3(5h) particles and corresponding EDS mappings of C, Al, O elements, respectively.

XRD patterns of the Al_2O_3 and C-Al_2O_3(5h) samples are shown in Figure 3.4. Carbon coating has resulted in the appearance of a broad XRD peak near 24°, characteristic of a disordered carbon.[30] A Raman spectrum of the C-Al_2O_3(5h) sample is shown in Figure 3.5. The most prominent feature of the spectrum being a sharp peak at about 1590 cm^{-1}. This peak corresponds most closely with the G band of single walled carbon nanotubes (SWCNT), which are commonly made by CVD processing.[31] Another sharp peak near 1480 cm^{-1} is close to the most prominent peak in the Raman spectrum of C_{60}.[32] The most prominent broad features near 1340 cm^{-1} and 1580 cm^{-1} correspond to the D and G bands of graphite.[33] The large D band compared to the G band indicating a highly disordered carbon.[34] Smaller broad features in the Raman spectrum could not be identified. These features and features similar to those of SWCNT, C_{60}, and disordered

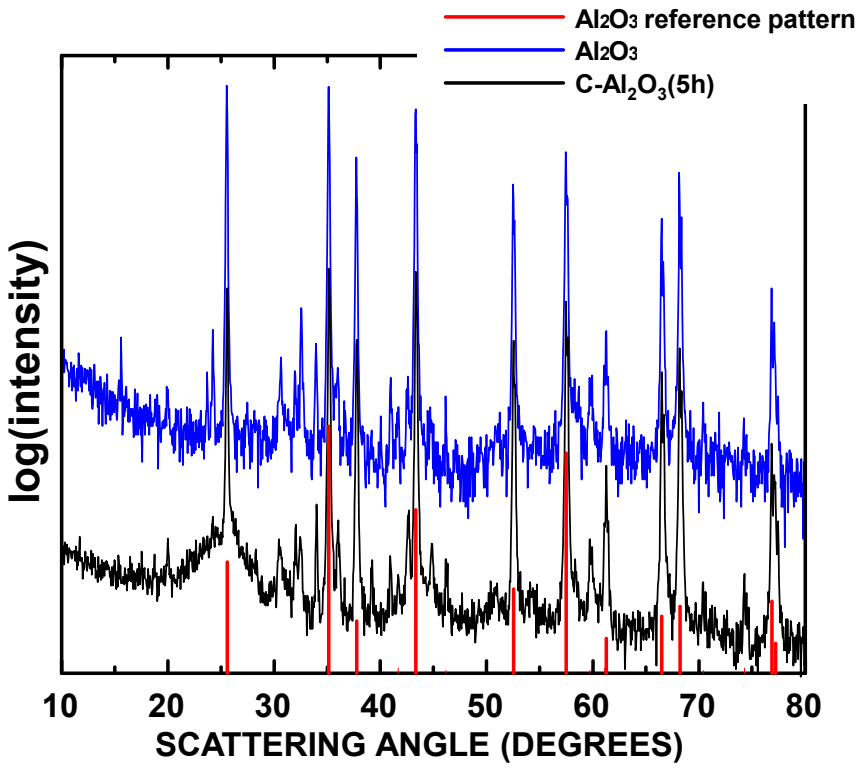

Figure 3.4 XRD patterns of Al_2O_3 and C-Al_2O_3(5h).

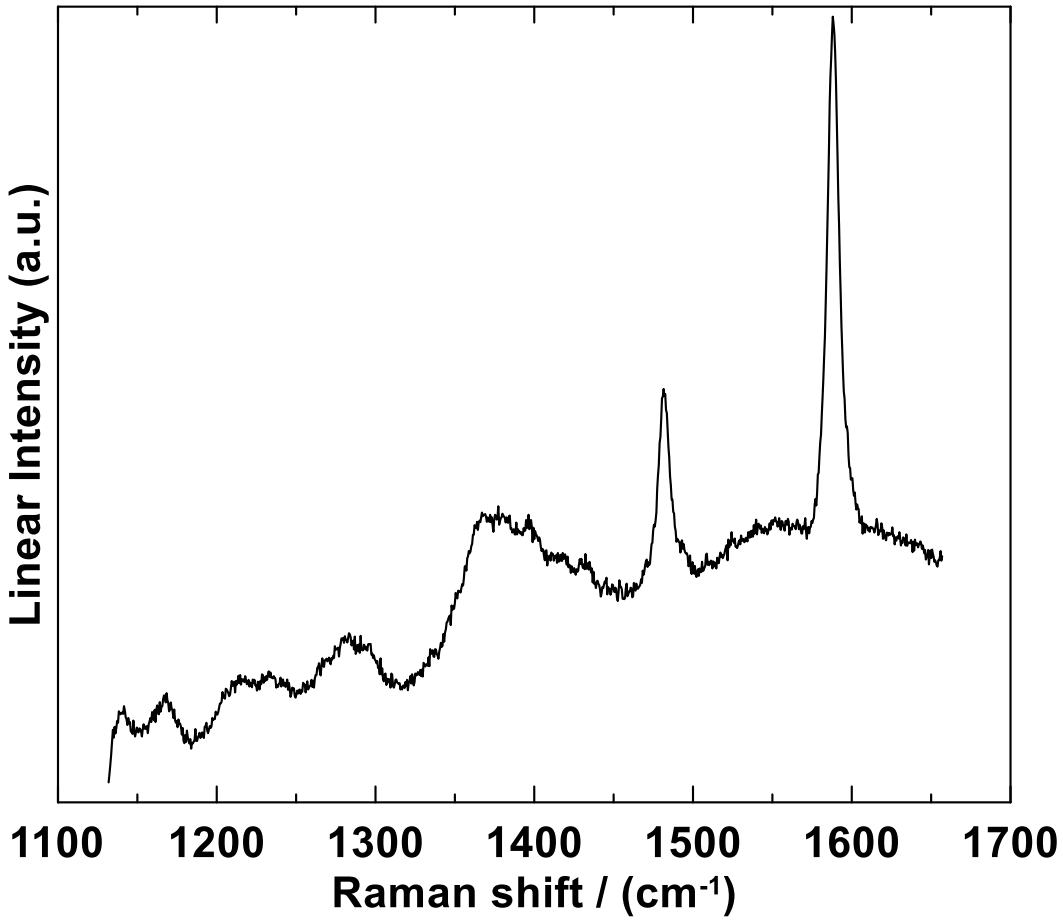

Figure 3.5 Raman spectrum of the C-Al2O3(5h) sample.

carbon suggest the deposited carbon is a complex mixture of metastable and disordered phases.

The C-Al_2O_3(5h) sample was used to determine the density, porosity, and electrochemical properties of the coated carbon. The amount of coating present on the C-Al_2O_3(5h) particles was determined to be 13 wt. % by thermogravimetric analysis (Figure 3.6). Helium pycnometry determined the C-Al_2O_3(5h) sample density to be 3.46 g/ml. From the TGA and pycnometry results, the density of coated carbon was calculated to be 1.84 g/ml. Assuming a uniform coating on the 0.39 m^2/g Al_2O_3 particles, a 13 wt. % 1.84 g/ml carbon coating corresponds to an average coating thickness of 0.2 μm, which is

consistent with SEM observations. The BET surface area of C-Al_2O_3(5h) was measured to be 0.50 m^2/g or 1.73 m^2/ml. This represents an 11% increase in volumetric surface area compared to the Al_2O_3 precursor particles. This higher value is likely due to the carbon coating that delaminated from the sample in some areas, as mentioned above, resulting in the formation of thin carbon flakes. Such thin flakes will have a high surface area and therefore their presence would cause an increase in overall surface area.

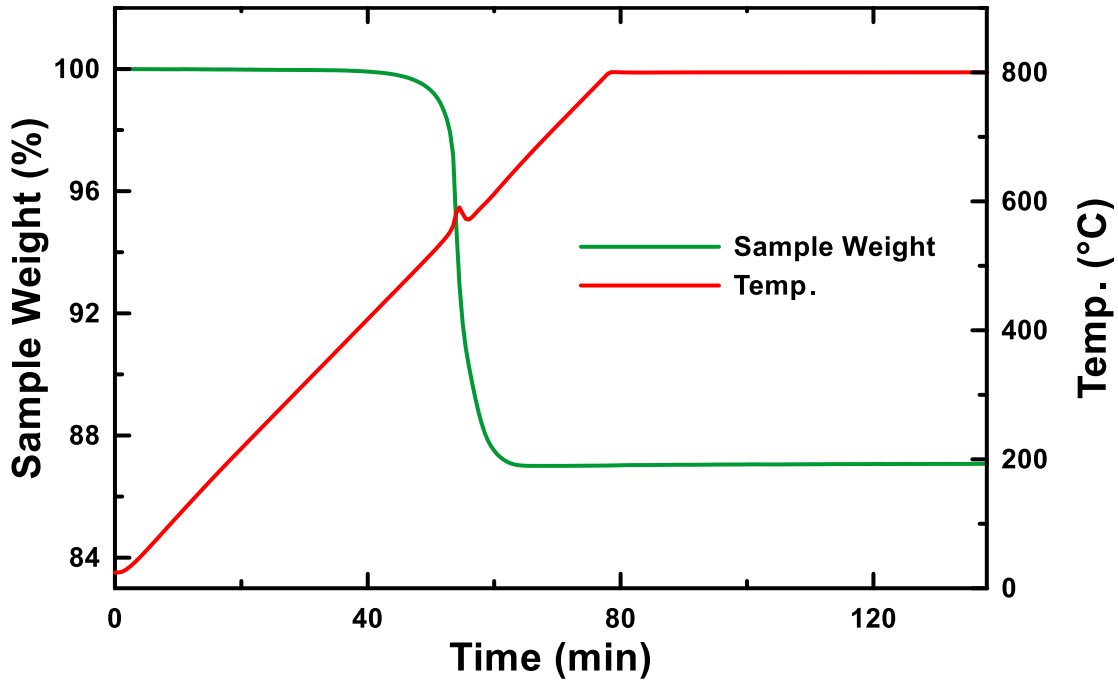

Figure 3.6 The weight loss of C-Al_2O_3(5h) during heating in air at a constant heating rate.

Since Al_2O_3 is electrochemically inactive in Li-cells, the C-Al_2O_3(5h) sample was used to evaluate the electrochemical properties of the carbon coating. Figure 3.7(a) shows the potential profile of C-Al_2O_3(5h). The profile is typical of a disordered carbon (i.e. either a hard carbon or partially pyrolyzed soft carbon, see for example Reference 35). The cycling performance is shown in Figure 3.7(b). The carbon coating has a specific

capacity of around 225 mAh/g, with no detectible loss of capacity and a high CE of 99.95% after 100 cycles.

Figure 3.8(a) shows an SEM image of uncoated graphite powder. The graphite particles are roughly spherical and are about 19 (D10) - 39 (D90) μm in size, with a median (D50) size of 27 μm. The true density of the graphite powder was measured to be 2.18 g/ml. This low value compared to the crystallographic density of graphite (2.26 g/ml) is indicative of internal porosity that is inaccessible to the helium gas used in the density measurement. The BET surface area of the graphite was measured to be 0.29 m^2/g. or 0.63 m^2/ml. The graphite particle surfaces are mostly smooth on the scale of the image shown in Figure 3.8(a), however ridges and pits in the surface are clearly visible. Figure 3.8(b) shows an SEM image of C-Gr(1h). The surface morphology has changed to nodular, with none of the features of the underlying graphite surface visible. Figure 3.8(c) shows an SEM image of C-Gr(2h). With extended carbon coating time, the nodules have elongated into spikes. In addition, the particles have begun to aggregate (Figure 3.9). Figure 3.8(d) shows an SEM image of a cross section of a C-Gr(2h) particle. The particles are completely coated with carbon, having an average coating thickness is about 1 μm.

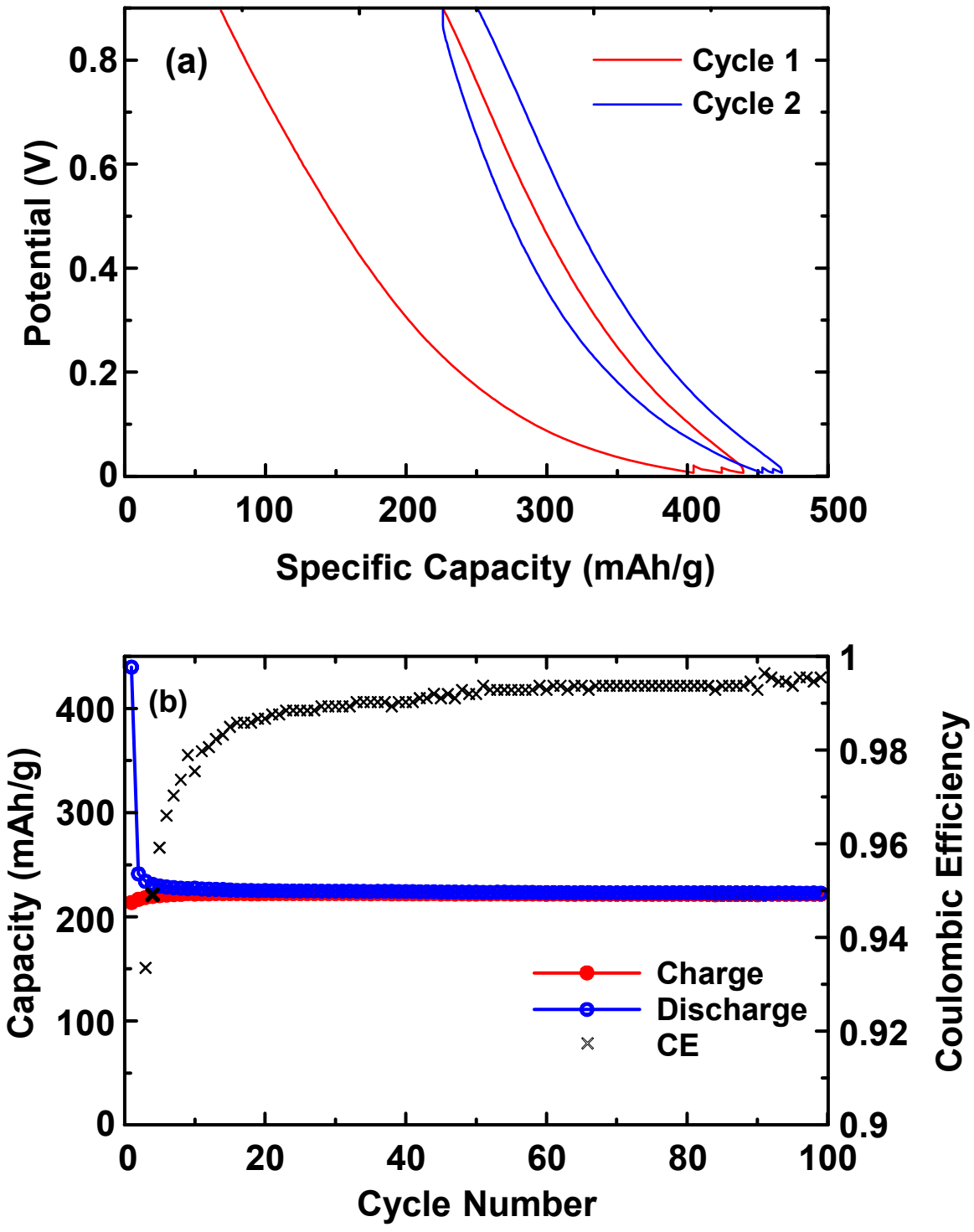

Figure 3.7 (a) Potential profile and (b) cycling performance of C-Al_2O_3(5h). Here the capacity is plotted in units of mAh per gram of carbon.

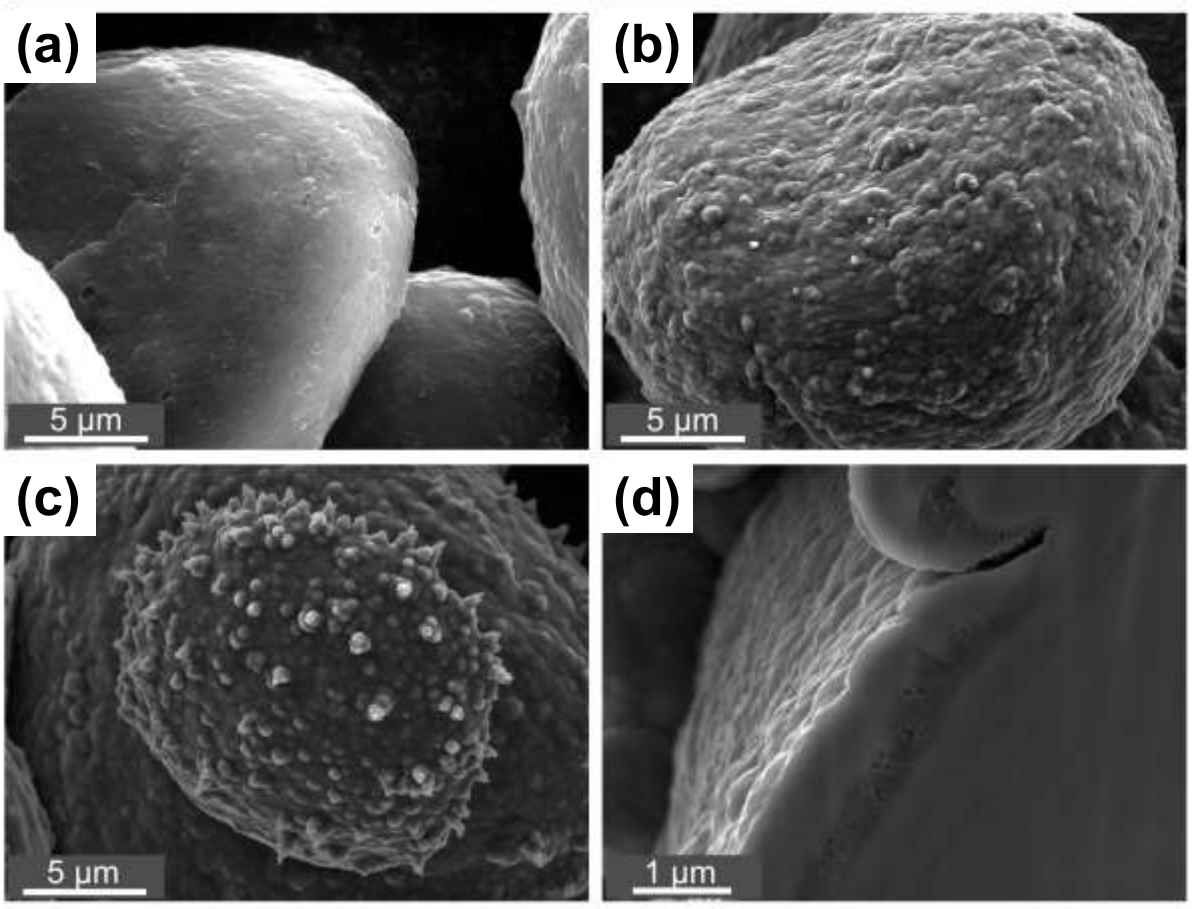

Figure 3.8 SEM images of (a) graphite, (b) C-Gr(1h), (c) C-Gr(2h), and (d) cross-sectioned C-Gr(2h).

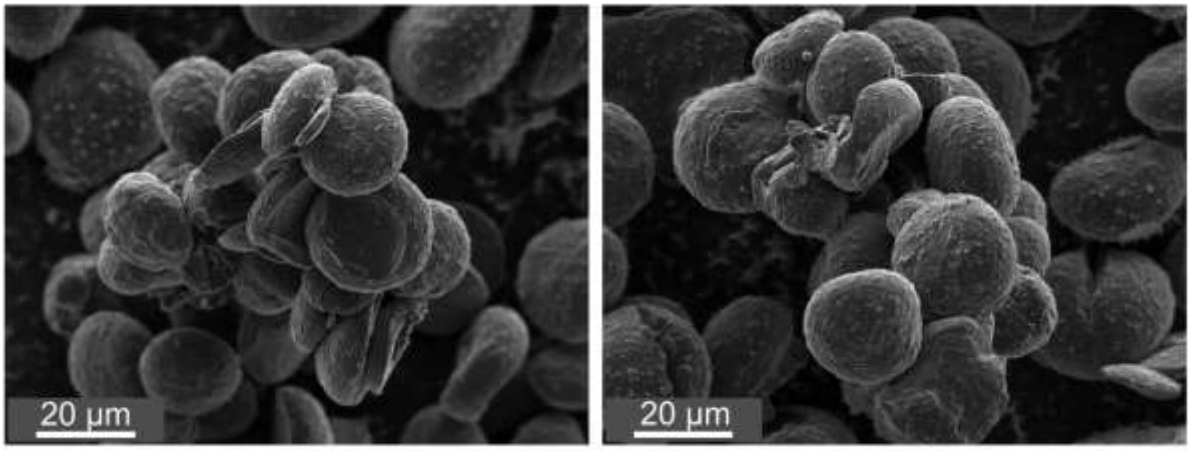

Figure 3.9 SEM images of C-Gr(2h) showing particle aggregation.

The BET surface area of the C-Gr(1h) particles was measured to be 0.2 m^2/g. This represents the lower limit of detection of the BET instrument, therefore the actual sample surface area may be even lower. Even so, this represents a considerable reduction (31%) compared to the surface area of the original graphite particles. We believe that this large reduction in surface area is due to a combination of the low surface area of the coated carbon plus the effect of pore closure. This can be seen in Figure 3.10, where internal porosity in the graphite has been closed off by the carbon coating. The density of the C-Gr(1h) particles was 2.14 g/ml. If the carbon coating has the same 1.84 g/ml density as determined from the C-Al_2O_3(5h) sample, this density reduction of the C-Gr(1h) compared to uncoated graphite corresponds to a 10% by weight carbon coating. After 2h of CVD processing, the density reduces further to 2.10 g/ml, corresponding to a 19% by weight carbon coating. Despite the formation of spiky nodules, the C-Gr(2h) sample's surface area remains near the lower detection limit of the BET instrument (0.19 m^2/g or 0.40 m^2/ml).

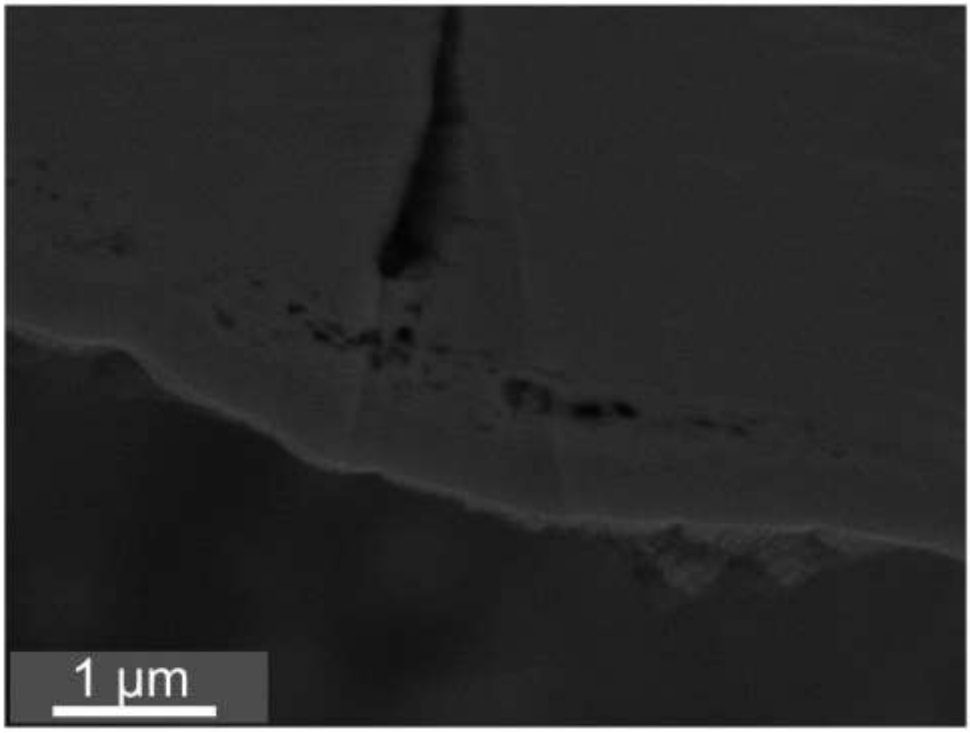

Figure 3.10 SEM image of a cross-sectioned C-Gr(2h) particle, showing pore closure due to the carbon coated layer.

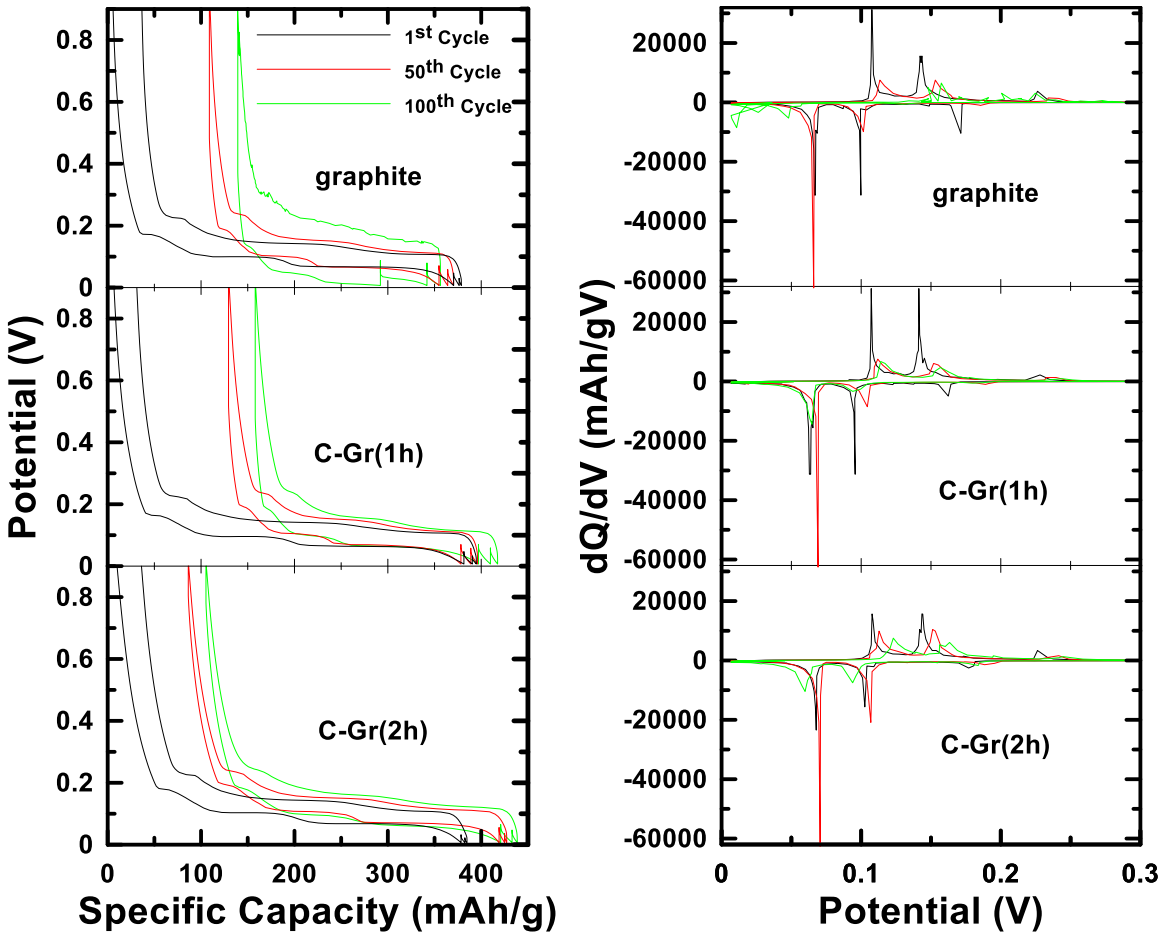

Figure 3.11 Potential profiles and differential capacity curves of graphite and C-Gr samples.

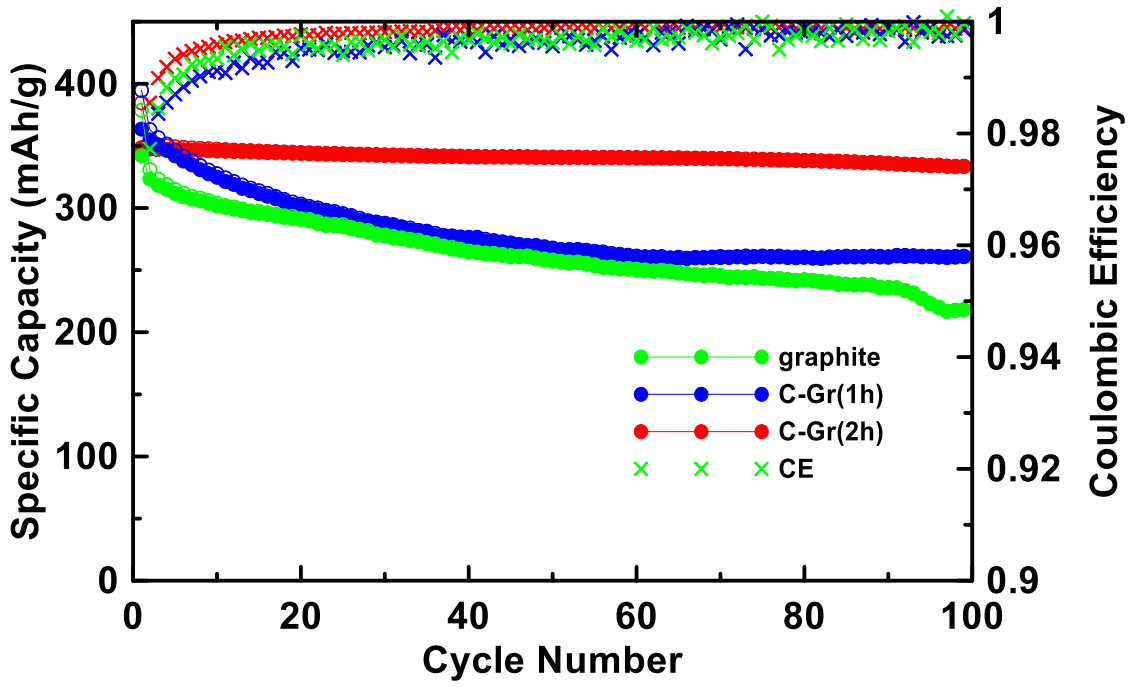

Figure 3.12 Cycling performance of graphite and C-Gr samples.

To evaluate the effectiveness of the carbon coating in improving the cycling characteristics of graphite in Li cells, graphite electrodes were made uncalendared and with low carbon black and binder content. Such coatings have poor electrical conductivity, resulting in exacerbated impedance growth. Figure 3.11 shows the potential profiles and differential capacity curves of the 1st, 50th and 100th cycle of graphite, C-Gr(1h), and C-Gr(2h) electrodes. Initially all potential profiles are similar and the differential capacity curves show distinct staging peaks. By cycle 50, there is capacity loss for the uncoated graphite and C-Gr(1h) with an increase in cell polarization, indicative of impedance growth, while the potential profile of C-Gr(2h) remains almost unchanged. By cycle 100, the polarization of the uncoated graphite electrode has become extremely severe and distinct staging plateaus are no longer visible, while the CVD coated electrodes have much less polarization and still show distinct staging plateaus.

These changes are evident in the capacity vs. cycle life of these electrodes, shown in Figure 3.12. All electrodes have a similar initial capacity of about 350 mAh/g. During cycling the uncoated graphite electrode suffers continual fade with ~35% loss in capacity after 100 cycles. As shown in Figure 3.11, this loss of capacity is due to increased polarization. The cycling of the C-Gr(1h) cell is only slightly improved. Both the graphite and C-Gr(1h) have similar coulombic efficiencies (CE, also shown in Figure 3.12), that increase during cycling, presumably improving as the SEI layer thickens. Evidently the 1h CVD coating was not sufficient to significantly impact SEI growth. In contrast, the C-Gr(2h) electrode shows almost no fade, little polarization growth, and a higher CE throughout cycling.

Despite the large differences in cell polarization observed during cycling, EIS spectra of the graphite, C-Gr(1h), and C-Gr(2h) samples (Figure 3.13) show relatively small differences in cell impedance. These spectra are typical of graphite electrodes, consisting of two semicircles, the first in the high frequency region being ascribed to lithium-ion diffusion through the SEI layer and the semicircle in the medium-to-low frequency being ascribed to the transfer resistance. The total real impedance of the C-Gr(2h) sample is slightly smaller than the C-Gr(1h) and graphite samples, but this is not significant enough to account for the large differences in polarization and fade observed in Figure 3.11 and 3.12. This indicates that the primary mechanism for failure in the graphite and C-Gr(1h) cells may be due to graphite exfoliation from solvent co-intercalation. This is known to increase cell polarization, but can simultaneously cause the graphite surface area to increase, resulting in little change or even a decrease in charge transfer resistance.[36] It is well known that carbon coating can effectively inhibit

solvent co-intercalation into graphite,[37] which is likely the primary mechanism by which polarization is reduced and cycling is improved in the C-Gr(2h) sample.

3.4 Conclusions

A lab-scale CVD apparatus has been developed with a fluidized bed that can efficiently contain small amounts (~3 ml, based on true density) of powdered samples in a furnace reaction zone. Furthermore, samples with different densities, particle shapes and particle sizes are contained in the reaction zone without any adjustment of the fluidized bed. The reactor was used to carbon coat a small (5 mL) sample of graphite particles, resulting in a uniform carbon coating that was shown to effectively inhibit electrolyte reactivity when the coated graphite was utilized as a negative electrode in Li cells. The ability to efficiently deposit continuous and even coatings onto small particle samples shown here presents a significant improvement over other CVD methods, which have difficulty processing small samples and in which the fluidized bed must be readjusted and optimized depending on powder properties. This presents an enormously useful tool for exploratory research in fields such as battery materials, where many small powder samples of active electrode materials must be synthesized for the investigation of trends in materials properties and for rapid materials optimization. In addition, this fluidized bed design can be used to synthesize unique composite materials, which we will be discussed in Chapter 5.

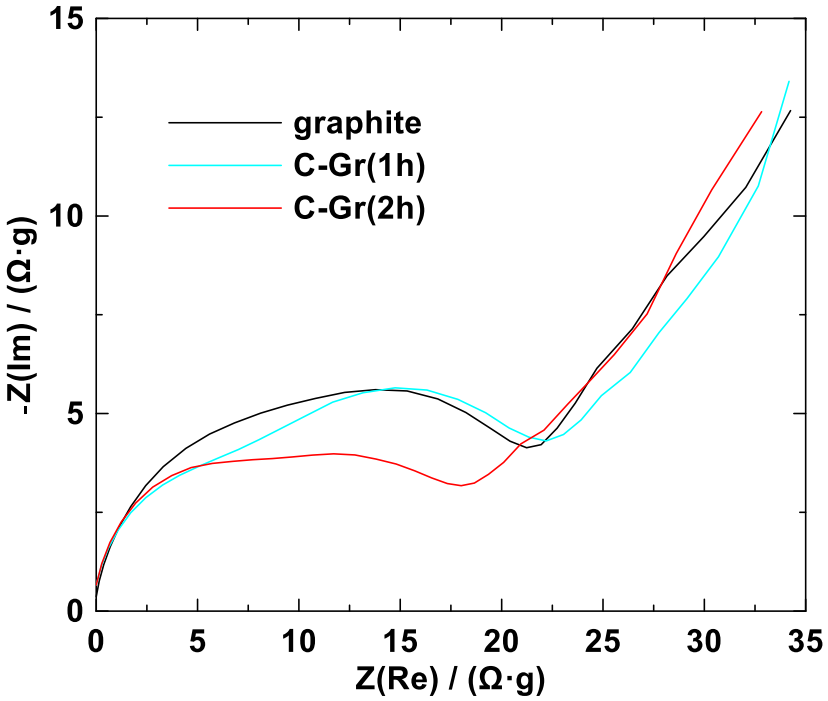

Figure 3.13 EIS spectra of graphite, C-Gr(1h) and C-Gr(2h) samples after 50 cycles measured at 0.9 V. The impedance values were multiplied by the active mass of the cell to take into account any differences in active loading.

CHAPTER 4 EVALUATION OF HYDROTHERMALLY CARBON COATED GRAPHITE IN LI-CELLS

4.1 Introdution

Graphite powders used as the active anode material of Li-ion batteries are often carbon coated to reduce reactivity with electrolyte, especially at exposed edges of the graphite basal planes on particle surfaces, which have relatively high reactivity with electrolyte. Utilization of uncoated graphite anodes can result in the accumulation of electrolyte reduction products over time, causing the solid electrolyte interphase (SEI) to thicken, increasing internal resistance and, consequently, reducing the cycle life.[38] Carbon coatings, typically applied by chemical vapor deposition (CVD) in the form of an amorphous carbon layer, can reduce surface reactivity significantly, resulting in reduced cell impedance and increased cycle life. Other methods to carbon coat graphite include spray pyrolysis, and sol-gel techniques.[17] However, each method has its own drawbacks, and creating a uniform and impermeable carbon coating is non-trivial. For instance, success of the CVD method requires that an efficient fluidized bed be created in the reaction zone of the furnace.[39] Even when this is established, CVD is highly inefficient, as substantial amounts of unreacted or partially reacted reactive gases are lost even under the best conditions.

Hydrothermal carbonization (HTC) is another method of coating particles with carbon that has been utilized for Li-ion battery materials, including $LiFePO_4$ cathodes and oxide/carbon and alloy/carbon composite anodes.[40-42] HTC involves the reduction of a soluble carbon source in a solvent as a reaction medium under elevated pressure and temperature. Water is commonly chosen as the solvent due to its low cost, environmental friendliness, and its ability to dissolve sugars as carbon sources. For the solute, any

water-soluble substance rich in carbon that does not introduce undesirable elements can typically be utilized. Glucose is a commonly used carbon source. When subjected to hydrothermal processing in aqueous solution at high temperatures (> 180 °C), glucose converts to hydrochar that coats any particles present in the solution.[43] As deposited, hydrochar is rich in oxygen and hydrogen. These elements can be removed by subsequent pyrolysis.

In this chapter, HTC was evaluated as a method for carbon coating Li-ion battery graphite. Despite many composite materials being reported, to the author's knowledge, the application of HTC for simply carbon coating graphite has not been reported. The physical and electrochemical properties of as-deposited and pyrolyzed HTC carbon were evaluated by depositing HTC carbon coatings onto an electrochemically inert powder. Al_2O_3 powder was utilized for this purpose. Graphite powder was then coated by HTC and the electrochemistry of the as-deposited and pyrolyzed carbon coated graphites were evaluated in Li cells.

4.2 Experimental

4.2.1 Hydrothermal Carbonization Procedure

10 grams of Al_2O_3 powder (600 mesh Aluminum Oxide Grit from Kramer Industries Inc.) or graphite powder (MesoCarbon MicroBeads, from China Steel Chemical Co., particle size ~26 microns), 10 grams of α-D-Glucose powder (anhydrous, 96%, from Sigma-Aldrich), and 150ml distilled water were loaded into the cylinder of a mini bench top hydrothermal reactor (Model 4560, Parr Instrument Company). The mixture was heated at 250 °C for 90 minutes while being stirred by a magnetic driven impeller at a speed of 100 RPM. During the reaction, pressures up to 5 MPa were

reached. After the desired processing time (eg. 5 hours), the reactor was gradually cooled to room temperature while stirring was maintained. Some pressure remained in the reactor after cooling, which was released via a needle valve prior to opening the reactor. Samples were carefully collected, washed, dried in air at 120 °C for 40 minutes, and then pyrolyzed in a tube furnace at 800°C for 3 hours under Ar. Carbon coated alumina and graphite samples are denoted here by "C-Al_2O_3(Xh)" and "C-Gr(Xh)", respectively, where the quantity in brackets is the processing time.

4.2.2 Material Characterization

X-ray diffraction (XRD) patterns were measured using a Rigaku Ultima IV powder diffractometer X-ray system equipped with a Cu Kα X-ray source, a diffracted beam monochromator, and a scintillation detector. Each XRD pattern was collected from 10° to 80° 2-theta in 0.05° increments for 3 seconds per step. Thermal gravimetric analysis (TGA) was conducted using a NETZSCH TG 209F3 thermogravimetric analyzer with compressed oxygen as purge gas (flow rate: 20 ml/min), in a heating range is from 20°C to 800°C with 10°C/min heating rate. Densities were measured with dry helium gas using a Micromeritics AccuPyc II 1340 gas pycnometer. Sample powder cross sections were prepared with a JEOL Cross-Polisher (JEOL Ltd., Tokyo, Japan) and sample powder morphologies were studied with a TESCAN MIRA 3 LMU variable pressure Schottky field emission scanning electron microscope (SEM) at 5.0 kV and 20.0 kV. BET surface areas were measured with dry nitrogen gas using a NOVA 4200e Analyzer. A summary of the coated carbon content, true density, and BET surface area of the samples prepared in this study is provided in Table 4.1.

Table 4.1 Coated carbon content, true density, and BET surface area of the samples prepared in this study.

Sample	Coated Carbon Content (wt %)	True Density (g/cm^3)	Surface Area (m^2/g)	Calculated Coated Layer Thickness (μm)
Al_2O_3	0%	3.98	0.35	N/A
C-Al_2O_3(20h)	11%	3.56	41	0.19
graphite	0%	2.18	0.28	N/A
C-Gr(5h)	14%	2.04	51	0.31

4.2.3 Electrochemical characterization

C-Al_2O_3(20h) electrode slurries were prepared from C-Al_2O_3(20h), carbon black (Super C65, Imerys Graphite and Carbon), and lithium polyacrylate (LiPAA) (from a 10 weight% LiPAA aqueous solution, made by neutralizing a polyacrylic acid solution (Sigma-Aldrich, average molecular weight of 250000 g per mol, 35 wt% in water) with $LiOH \cdot H_2O$ (Sigma Aldrich, 98%)) in a volumetric ratio of 70/5/25 (corresponding to a 83/4/13 weight ratio) with a few drops of wetting agent (isopropanol, Sigma-Aldrich, 99.5%) in distilled water. C-Gr(5h) electrode slurries were prepared from C-Gr(5h), carbon black, and polyvinylidene fluoride binder (PVDF, Kynar HSV 900) in a mass ratio of 90/5/5 with an appropriate amount of N-methyl-2-pyrrolidone (NMP, Sigma Aldrich, anhydrous 99.5%) to establish a good slurry viscosity. Slurries were mixed using a high-shear mixer equipped with a Cowles blade at 5000 rpm for 10 min. and then spread onto electrolytic copper foil (Furukawa Electric, Japan) with a 0.1 mm gap coating bar. The coatings were dried in air at 120 °C for 40 min., punched into 1.3 cm (in diameter) disks, and then heated under vacuum for a few hours at 120 °C with no further air exposure before cell assembly.

Electrodes were assembled into 2325-type coin cells with a lithium foil (Aldrich, 99.9%) counter/reference electrode separated by two layers of separators (Celgard 2300) in an Argon filled glove box. 168 μL of electrolyte was used in each half cell. The electrolyte consisted of 1M $LiPF_6$ (BASF) in a solution of ethylene carbonate (EC), diethyl carbonate (DEC), and mono-fluoroethylene carbonate (FEC) (volume ratio 3:6:1, all from BASF) for C-Al_2O_3(20h) and 1M $LiPF_6$ in a solution of propylene carbonate (PC), ethylene carbonate (EC), and diethyl carbonate (DEC) (volume ratio 6:10.5:5.5, all from BASF) for C-Gr(5h). Cells were cycled at 30 °C between 7 mV and 0.9 V using a Neware battery testing system at a C/10 rate for the 1st cycle and a C/5 rate for the following cycles. Cells were held at 7 mV after discharge (lithiation) until a rate decreased to C/20 for the first cycle or C/10 for subsequent cycles, to simulate CCCV charging in a full cell.

4.3 Results and discussion

Figure 4.1 shows SEM images of the result of carbon coating Al_2O_3 particles by HTC. Uncoated Al_2O_3 particles are shown in Figure 4.1(a) for comparison. The uncoated Al_2O_3 particles are about 9 μm (D10) - 20 (D90) μm in size, with a median (D50) size of 14 μm. The particles are dense, irregularly shaped, with smooth sides and sharp edges. The BET surface area of these particles was measured to be 0.35 m^2/g or 1.39 m^2/ml (as determined from the BET surface area and a measured density of 3.98 g/ml). Figure 1(b) is an SEM image of C-Al_2O_3(20h) particles, which are uniformly covered with a thick carbon layer that considerably rounds the edges of the particles, compared to the uncoated sample. Figure 4.1(c) shows an SEM image of cross-sectioned C-Al_2O_3(20h) particles. The particles consist of an Al_2O_3 core with a that is completely coated with a

carbon layer that is around 0.5 – 0.9 μm in thickness. At the top half of the SEM image is adhesive from the carbon tape used to mount the sample. On the bottom half of the particles there is an additional layer of Al_2O_3 on the particles. This is an artifact of back sputtering during the ion milling process. The back sputtering direction was towards the top of the image. Therefore, the top-half of the particles were shadowed from back sputtering and were unaffected. EDS maps of C, Al, and O (Figure 4.1(d-f), respectively) more clearly show the full encapsulation of the Al_2O_3 particles within a pure carbon (and the shadowing effect of the back sputtered Al_2O_3 artifact). XRD patterns of the Al_2O_3 and C-Al_2O_3(20h) samples are shown in Figure 4.2. They are plotted on a log scale, so that any amorphous carbon present is more visible in the patterns. The major peaks in the XRD patterns are due to Al_2O_3. Many smaller impurity peaks that could not be identified are highlighted on this log scale. The C-Al_2O_3(20h) sample has a broad XRD peak near 24°, characteristic of a disordered carbon, that is not present in the XRD pattern of uncoated Al_2O_3. Therefore, this peak is thought to be due to the carbon deposited on the surface, which has an amorphous character.

The C-Al_2O_3(20h) sample was used to determine the density, and electrochemical properties of the coated carbon. The amount of coating present on the C-Al_2O_3(20h) particles was determined to be 11 wt. % by thermogravimetric analysis (Figure 4.3). Helium pycnometry determined the C-Al2O3(20h) sample density to be 3.56 g/ml. From the TGA and pycnometry results, the density of coated carbon was calculated to be 1.89 g/ml. Assuming a uniform coating on the 0.35 m^2/g Al_2O_3 particles, a 11 wt. % 1.89 g/ml carbon coating corresponds to an average coating thickness of 0.19 μm, which is not

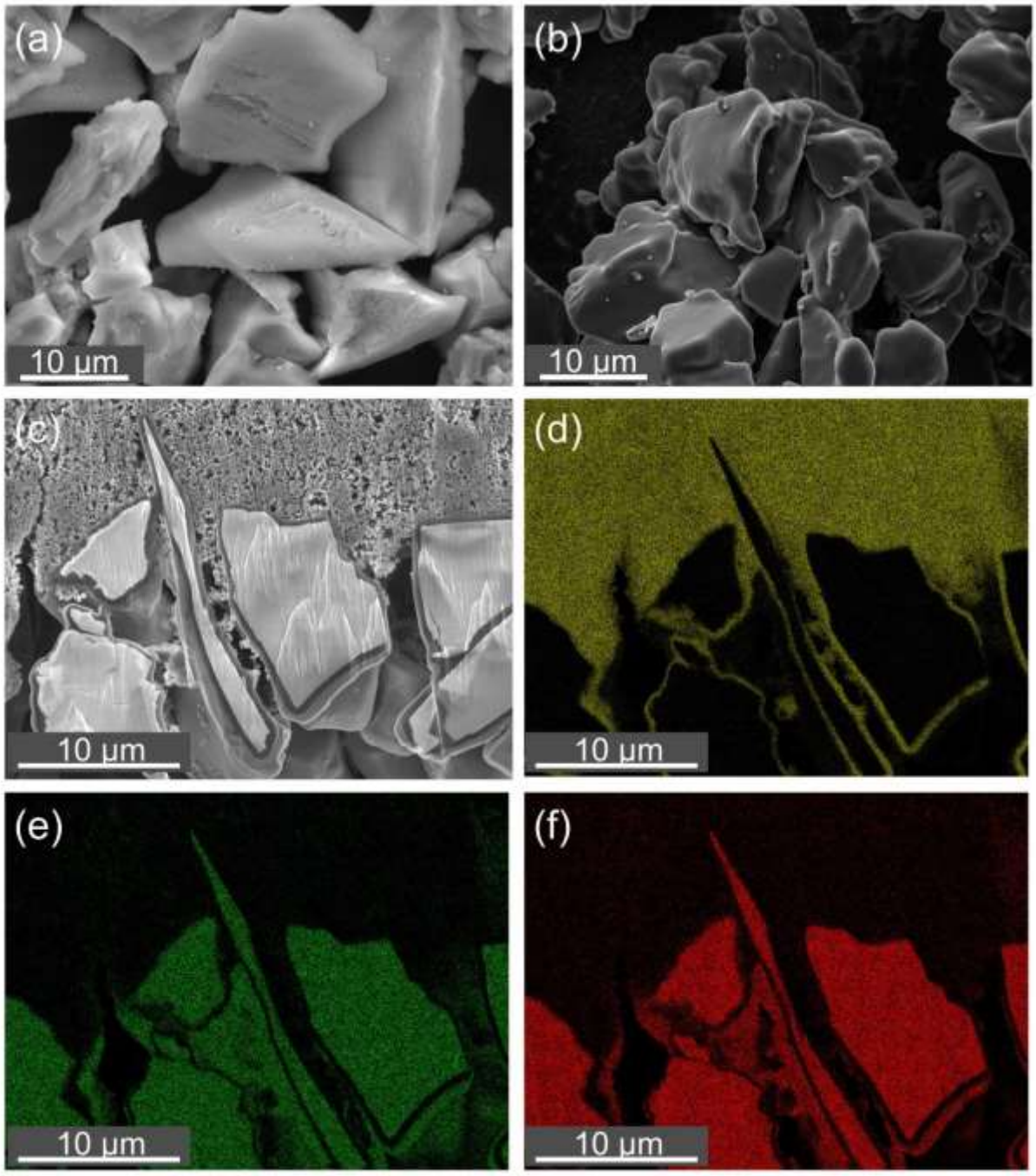

Figure 4.1 SEM images of (a) uncoated Al_2O_3 powder, and (b) C-Al_2O_3(20h). (c-f) SEM images of cross-sectioned C-Al_2O_3(20h) particles and corresponding EDS mappings of C, Al, O elements, respectively.

consistent with SEM observations. This inconsistency is explained when surface area measurements are taken into account. The BET surface area of C-Al_2O_3(20h) was measured to be 41 m^2/g or 146 m^2/ml. This is almost 120 times larger in surface area compared to the Al_2O_3 precursor particles. To cause this increase in surface area, the surface area of the carbon coating must be about 370 m^2/g. This indicates that the carbon layer is highly porous which, in turn, explains why the observed (0.5 μm – 0.9 μm) coating thickness is much larger than that calculated assuming that the layer has zero porosity (0.2 μm).

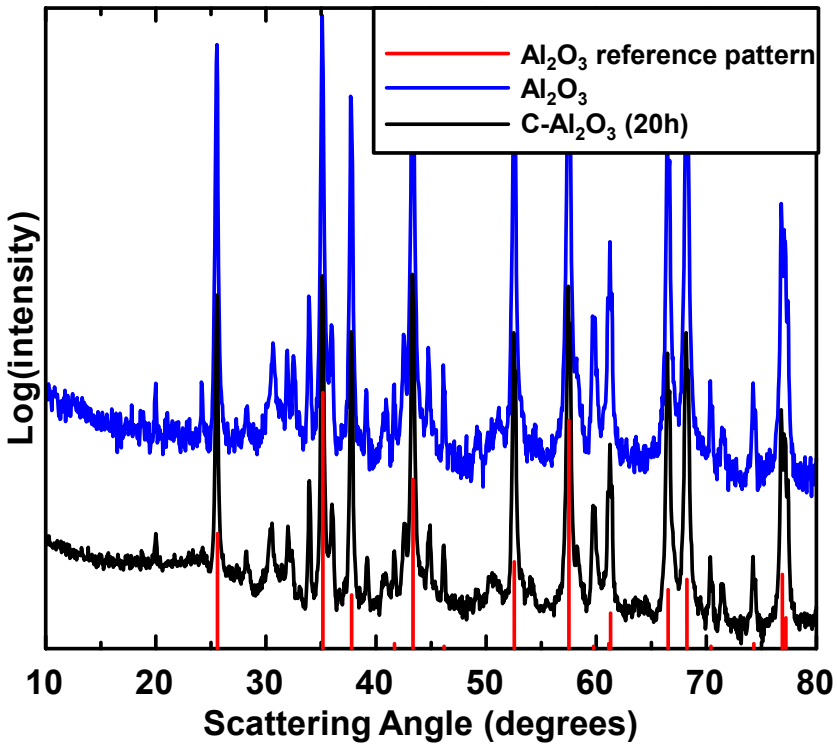

Figure 4.2 XRD patterns of Al_2O_3 and C-Al_2O_3(20h).

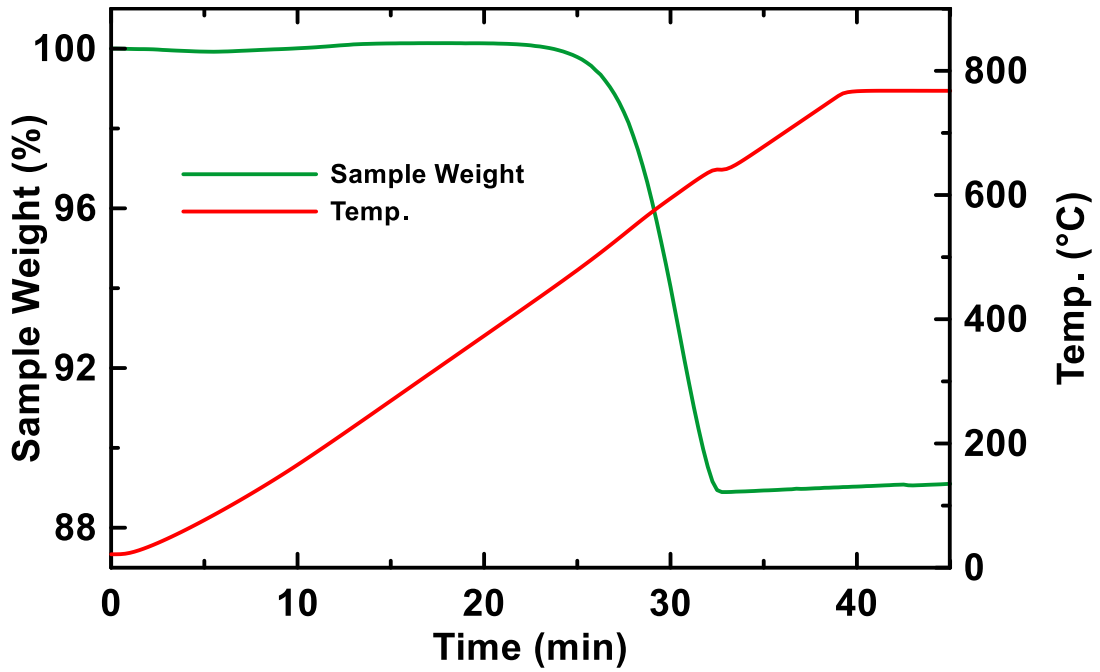

Figure 4.3 The weight loss of C-Al_2O_3(20h) during heating in oxygen at a constant heating rate.

Since Al_2O_3 is electrochemically inactive in Li-cells, the C-Al_2O_3(20h) sample was used to evaluate the electrochemical properties of the carbon coating. Figure 4.4 shows the potential profile of C-Al_2O_3(20h). The profile is sloping with no discernable plateaus. The first cycle comprises a large first lithiation capacity of 832 mAh/g and an initial coloumbic efficiency of only 28 %. Subsequent cycles have a capacity of about 230 mAh/g with little fade a high CE, reaching 99.3% in the 100 cycles shown. This potential profile is typical of a disordered carbon (i.e. either a hard carbon or partially pyrolyzed soft carbon, see for example Reference 35).

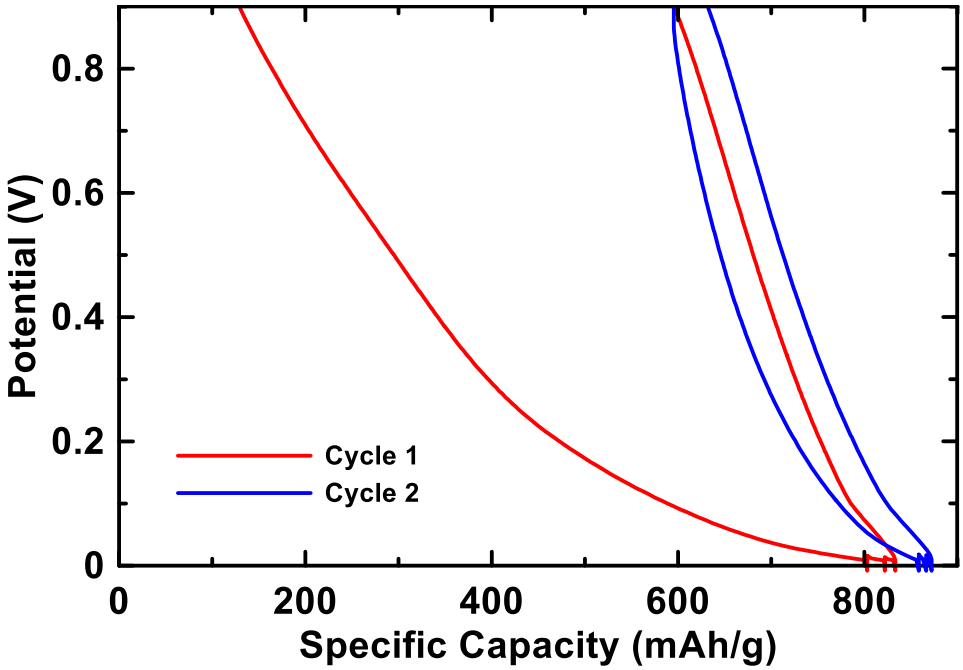

Figure 4.4 Potential profile of C-Al_2O_3(20h). Here the capacity is plotted in units of mAh per gram of carbon.

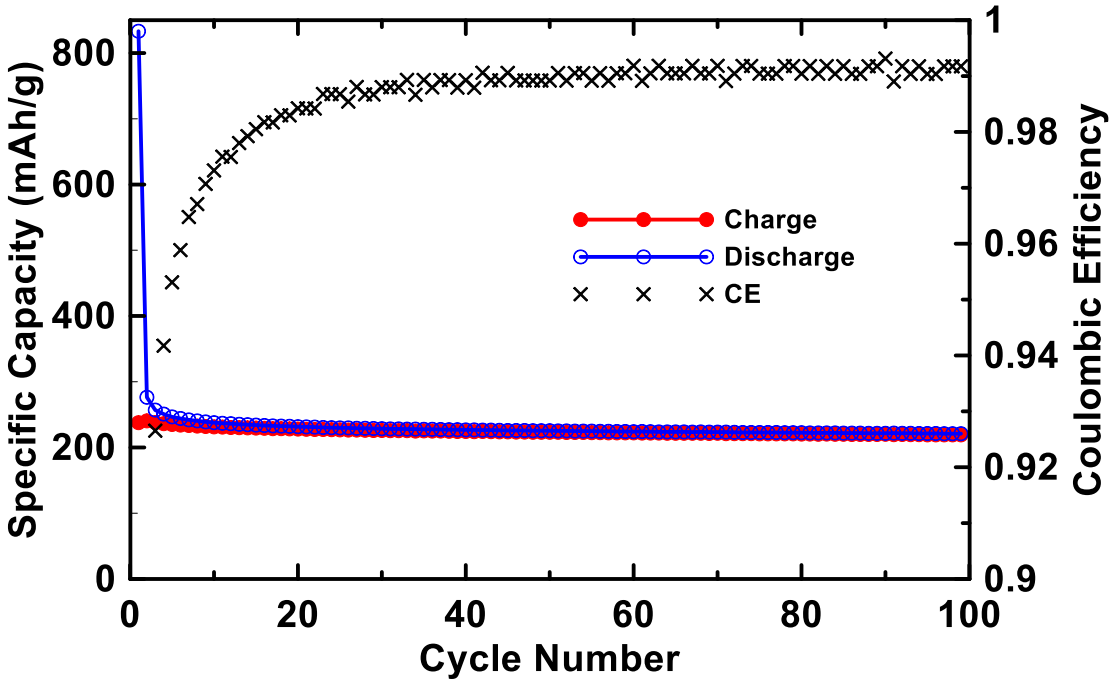

Figure 4.5 Cycling performance of C-Al_2O_3(20h). Here the capacity is plotted in units of mAh per gram of carbon.

Figure 4.6(a) shows an SEM image of uncoated graphite powder. The graphite particles are roughly spherical and are about 19 (D10) - 39 (D90) μm in size, with a median (D50) size of 27 μm. The density of the graphite powder was measured by helium pycnometry to be 2.18 g/ml. This low value compared to the crystallographic density of graphite (2.26 g/ml) is indicative of internal porosity that is inaccessible to the helium gas used in the density measurement. The BET surface area of the graphite was measured to be 0.28 m^2/g. or 0.61 m^2/ml. The graphite particle surfaces are mostly smooth on the scale of the image shown in Figure 4.6(a), however ridges and pits in the surface are clearly visible.

Figure 4.6(b) shows an SEM image of C-Gr(5h). The surface morphology has changed to being smooth and nodular, with none of the features of the underlying graphite surface visible. Figure 4.6(c) shows an SEM image of a cross section of a C-Gr(5h) particle. The lighter shades of grey in the image are graphite and the darker shades represent the carbon coating. The average carbon coating thickness is about 0.7 μm - 1 μm. This thickness remains constant even between particles that have been fused together by the HTC process. some of the isolated internal porosity of the graphite particles is also visible in this image.

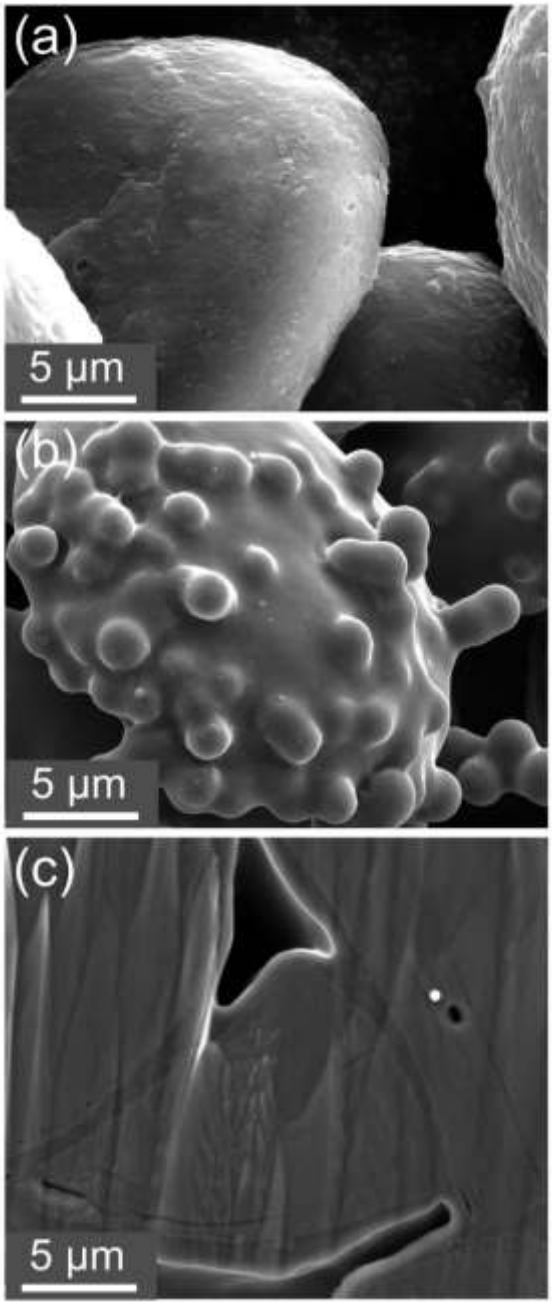

Figure 4.6 SEM images of (a) graphite, (b) C-Gr(5h), and (c) cross-sectioned C-Gr(5h).

The BET surface area of the C-Gr(5h) particles was measured to be 51 m^2/g. This is 180 times larger compared to the surface area of the original graphite particles, again indicating that the coated carbon layer is highly porous. The density method used to

calculate the coated carbon content for the C-Al_2O_3(20h) sample could not be used for the C-Gr(5h) due to the above mentioned error in density measurement of graphite due to isolated internal porosity. Therefore, an estimate of the coated carbon content was made by assuming a coated carbon surface area was the same as that of the C-Al_2O_3(20h) sample (370 m^2/g) and from this determining the amount of coated carbon needed to cause a surface area increase from 0.28 m^2/g observed for the uncoated graphite to a value of 370 m^2/g for C-Gr(5h). This gave the result that the coated carbon accounts for about 14 % of the C-Gr(5h) sample mass.

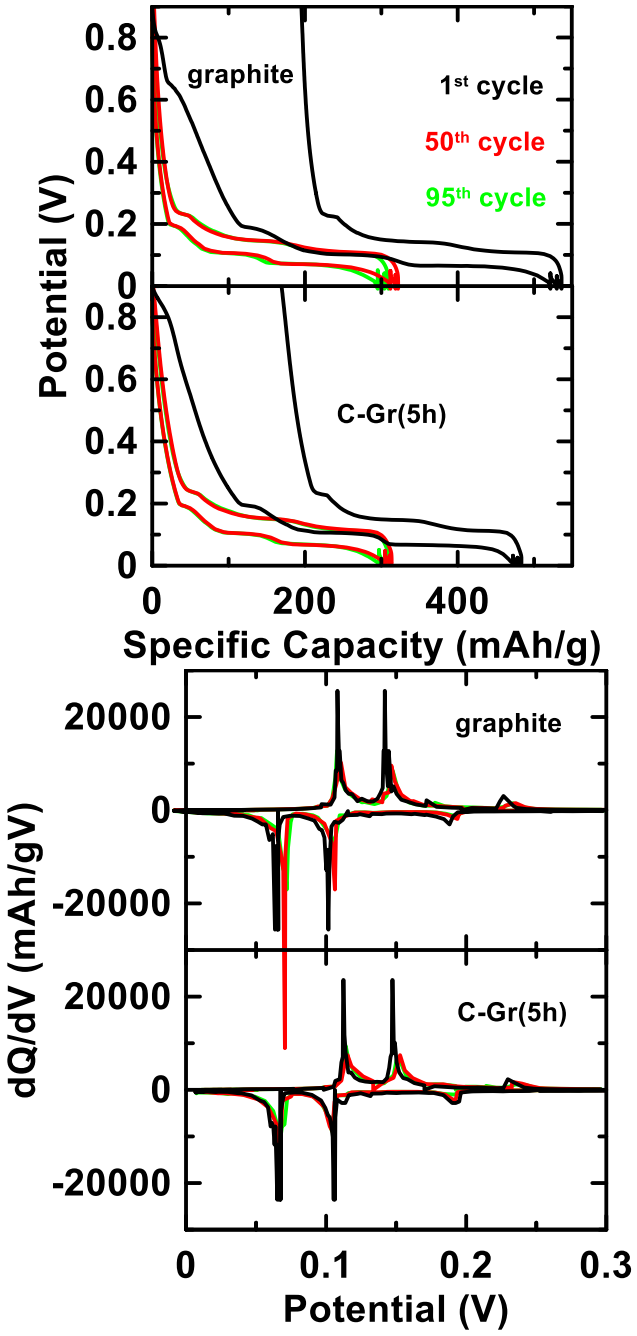

Figure 4.7 Potential profiles and differential capacity curves of graphite and C-Gr(5h) samples.

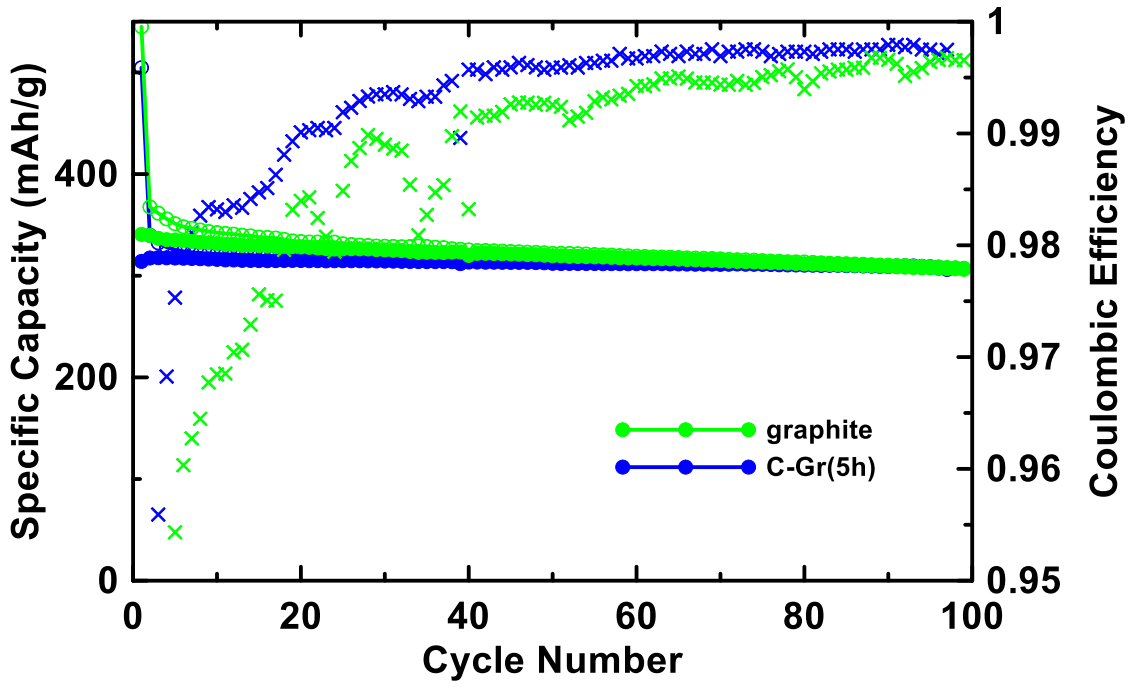

Figure 4.8 Cycling performance of graphite and C-Gr(5h) samples.

To evaluate the effectiveness of the carbon coating in improving the cycling characteristics of graphite in Li cells, an electrolyte containing propylene carbonate (PC) was selected because PC is known to co-intercalate into graphite, causing exfoliation and loss of capacity.[44] Figure 4.7 shows the potential profiles and differential capacity curves of the 1st, 50th and 95th cycle of graphite and C-Gr(5h) electrodes. Initially all potential profiles are similar and the differential capacity curves show distinct staging peaks. The large irreversible capacity during the first cycle can be attributed to SEI growth and co-intercalation of the PC solvent. By cycle 50, there is a small capacity loss for the graphite while the C-Gr(5h) capacity remains almost unchanged. This trend continued till to the 100th cycle. These changes are more evident in Figure 8, which shows a plot of the capacity vs. cycle life of these electrodes. During cycling, the graphite electrode suffers continual fade with ~10% loss in capacity after 100 cycles and low values of the CE,

especially in the first 10 cycles. In contrast, the C-Gr(5h) electrode had higher CE during cycling and lost only ~5% of its capacity during the 100 cycles shown. This indicate that the carbon coating is effective at reducing surface reactivity.

4.4 Conclusions

The hydrothermal carbonization method was evaluated for applying carbon coatings to graphite for Li cells. After hydrothermal carbonization and heating to 800 °C, a uniform carbon coating was observed to form on Al_2O_3 particles. The coating was highly porous, having a surface area of 370 m^2/g and its electrochemical properties were found to be typical of a hard carbon or partially pyrolyzed soft carbon. After hydrothermal carbonization and heating to 800 °C, a continuous, but nodular carbon coating was observed to form on graphite particles. The deposited carbon was found to have low density and porous. Nevertheless, the layer was shown to be effective at reducing surface reactivity with electrolyte in Li-cells, resulting in improved coulombic efficiency and capacity retention during cycling. Considering this, and the relative ease of utilizing the hydrothermal carbonization method compared to other surface coating methods (e.g. CVD), hydrothermal carbonization presents a highly attractive method for carbon coating Li-ion battery graphites.

CHAPTER 5 EXPLORATION OF NEW MATERIALS SYNTHESES

5.1 Introduction

As mentioned in Chapter 3, Chemical vapor deposition (CVD) is a widely used method of making new materials. A typical rotary CVD furnace is particularly useful for continuous processing to deal with large amounts of powder material by controlling the rotation speed, gas flow, and tipping angle. However, for larger diameter commercial CVD rotary tubes, the powder material tends to slide in the tube more than it is agitated and tumbled. This problem was solved by adding two opposing screws and lifter bars in a small diameter reaction tube, as shown in Chapter 3, enabling lab-scale CVD onto a fluidized powder bed. This solution represents an entirely new method of CVD. Therefore, how powders behave and how they are coated in this apparatus are entirely unknown.

The mechanofusion method developed for lithium-ion batteries material research in our group has also been investigated in this thesis. The mechanofusion method can spheronize particles, reduce materials surface area, and eliminate the surface features on particles.[45] It also has the ability to coat small particles onto big particles, to produce coated particles for lithium-ion batteries.[46] Despite the versatility of this method, not many studies have been published on its use. The effect of many factors on processing dynamics and product formation: like material loading, drum speed, press head gap, temperature, etc. remain virtually unexplored.

Because of the many unknowns in the CVD and mechanofusion methods, initial exploratory experiments were conducted to see what these methods could do under

different conditions. This chapter describes some of these experiments and, in some cases, the properties of the unique materials that resulted from them.

5.2 Synthesis of Spherical Si-alloy/Carbon Composites in an Opposing Screw CVD Reactor

5.2.1 Introduction

In attempting to carbon coat Si-alloy powders utilizing the opposing screw CVD reactor described in Chapter 3, it was found that often the alloy particles would aggregate in the CVD reactor such that spherical Si-alloy/carbon composites were produced. Although the formation of such composites was not the intention, their resulting microstructure was attractive and such composites exhibited good cycling characteristics in Li cells. This section will describe one example of the synthesis and characterization of a spherical Si-alloy/carbon composite made in an opposing screw CVD reactor.

5.2.2 Experimental

5 mL of commercial silicon alloy powder (3M V7 fine powder) was placed at the center of the furnace tube of the opposing screw CVD reactor described in Chapter 3. The loaded tube was assembled according to the CVD operation process described in Chapter 3 and was purged with Ar gas (60 ml/min.) for 1 hour. While still under Ar-gas flow, tube rotation was started at ~100 rpm and the temperature was increased to 800°C in 30 minutes. The Ar gas flow was then stopped, and a flow of ethylene gas was established through the tube at 80 ml/min. for 2 hours, while the tube was under constant rotation and heated at 800°C. The flow of ethylene gas was then stopped, Ar was reintroduced in the tube at 60 ml/min., and the furnace was allowed to cool. Rotation was stopped only after the sample reached room temperature. Half the sample (referred to here as C-V7(2h)) was carefully collected from the furnace tube without contamination from accumulated

downstream tar. The other half of the sample (referred to here as C-V7(5h)) was recoated for 3 more hours in the CVD reactor under same operation conditions. Sample powder cross sections were prepared using an ion mill (IB-19530CP, JEOL Ltd., Tokyo, Japan) and sample powder morphologies were studied with by SEM (TESCAN MIRA 3 LMU variable pressure Schottky field SEM) at 5.0 kV and 20.0 kV.

Electrode slurries were prepared from the coated samples, carbon black (Super C65, Imerys Graphite and Carbon), and polyvinylidene fluoride binder (PVDF, Kynar HSV 900) in a mass ratio of 90/5/5 with an appropriate amount of N-methyl-2-pyrrolidone (NMP, Sigma Aldrich, anhydrous 99.5%) to establish a good slurry viscosity. Slurries were mixed using a high-shear mixer equipped with a Cowles blade at 5000 rpm for 10 min. and then spread onto electrolytic copper foil (Furukawa Electric, Japan) with a 0.1 mm gap coating bar. The coatings were dried in air at 120 °C for 40 min., punched into 1.3 cm (in diameter) disks, and then heated under vacuum for a few hours at 120 °C with no further air exposure before cell assembly.

Electrodes were assembled into 2325-type coin cells with a lithium foil (Aldrich, 99.9%) counter/reference electrode separated by two layers of separators (Celgard 2300) in an Argon filled glove box. 168 μL of electrolyte was used in each half cell. The electrolyte consisted of 1M $LiPF_6$ (BASF) in a solution of ethylene carbonate (EC), diethyl carbonate (DEC), and with or without mono-fluoroethylene carbonate additive (FEC) (volume ratio 3:6:1, all from BASF). Cells were cycled at 30 °C between 7 mV and 0.9 V using a Neware battery testing system at a C/10 rate for the 1st cycle and a C/5 rate for the following cycles. Cells were held at 7 mV after discharge (lithiation) until

their rate decreased to C/20 for the first cycle or C/10 for subsequent cycles, to simulate CCCV charging in a full cell.

5.2.3 Results and Discussion

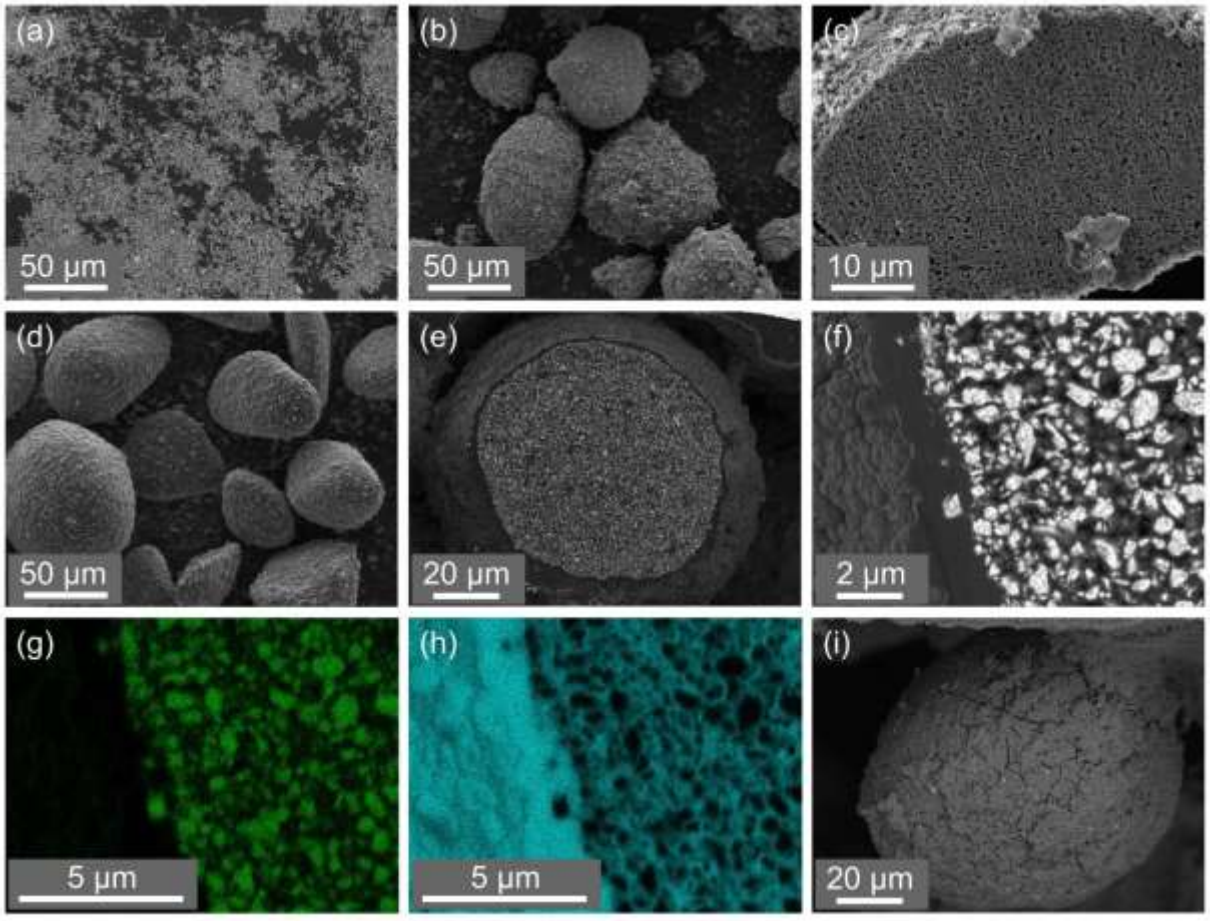

Figure 5.1 (a) SEM image of 3M-V7 powder; (b) SEM image of C-V7(2h); (c) Cross-section image of C-V7(2h); (d) SEM image of C-V7(5h); (e) Cross-section image of C-V7(5h); (f),(g),and (h) SEM image and EDS mapping of C-V7(5h) and Si, C element in C-V7 (5h); (i) SEM image of C-V7(5h) after 100 cycles.

Figure 5.1(a) shows an SEM image of uncoated 3M V7 powder. It consists of submicron particles having an average particle size of about 0.5 μm. After 2 hours of carbon coating procedure the C-V7(2h) sample was formed. In this sample, the V7 alloy powder aggregated into much bigger (~50 μm) secondary particles, as shown in Figure

5.1(b) 50 μm. A cross-section image of a C-V7(2h) particle is shown in Figure 5.1(c). The particle is highly porous. It consists of aggregated alloy particles, with little evidence of deposited carbon. Figure 5.1(d,e) show SEM images of the C-V7(5h) sample and its cross section. In this sample, a layer of carbon coating is visible on each particle and a thick ~1 μm outerlayer of carbon has formed on the surface of the secondary particles. This structure is further confirmed from enlarged cross-section maps of Si and C (Figure 5.1(f,g,h)), which clearly show that a carbon coating exists around each individual alloy particle and, additionally, around the entire particle. This microstructure is attractive, as the outerlayer may afford protection for the alloy surfaces from reaction with the electrolyte.

Figure 5.2 shows the cycling performance of V7 compared C-V7(2h) and C-V7(5h) in lithium cells with and without FEC additive. With the electrode and electrolyte formulations used here, V7 alloy fades rapidly. A significant improvement in cycling performance is observed for the C-V7(2h) sample and a further improvement in cycling performance is observed for the C-V7(5h) sample. This suggests that such a microstructure may be useful for improving the cycle life of Si-based anodes. However, since FEC is observed to improve cycling for all of the materials tested, this suggests that the alloy is still in contact with the electrolyte. Further improvements are needed if these materials are to be used as to be drop-in replacements for graphite in Li-ion cells.

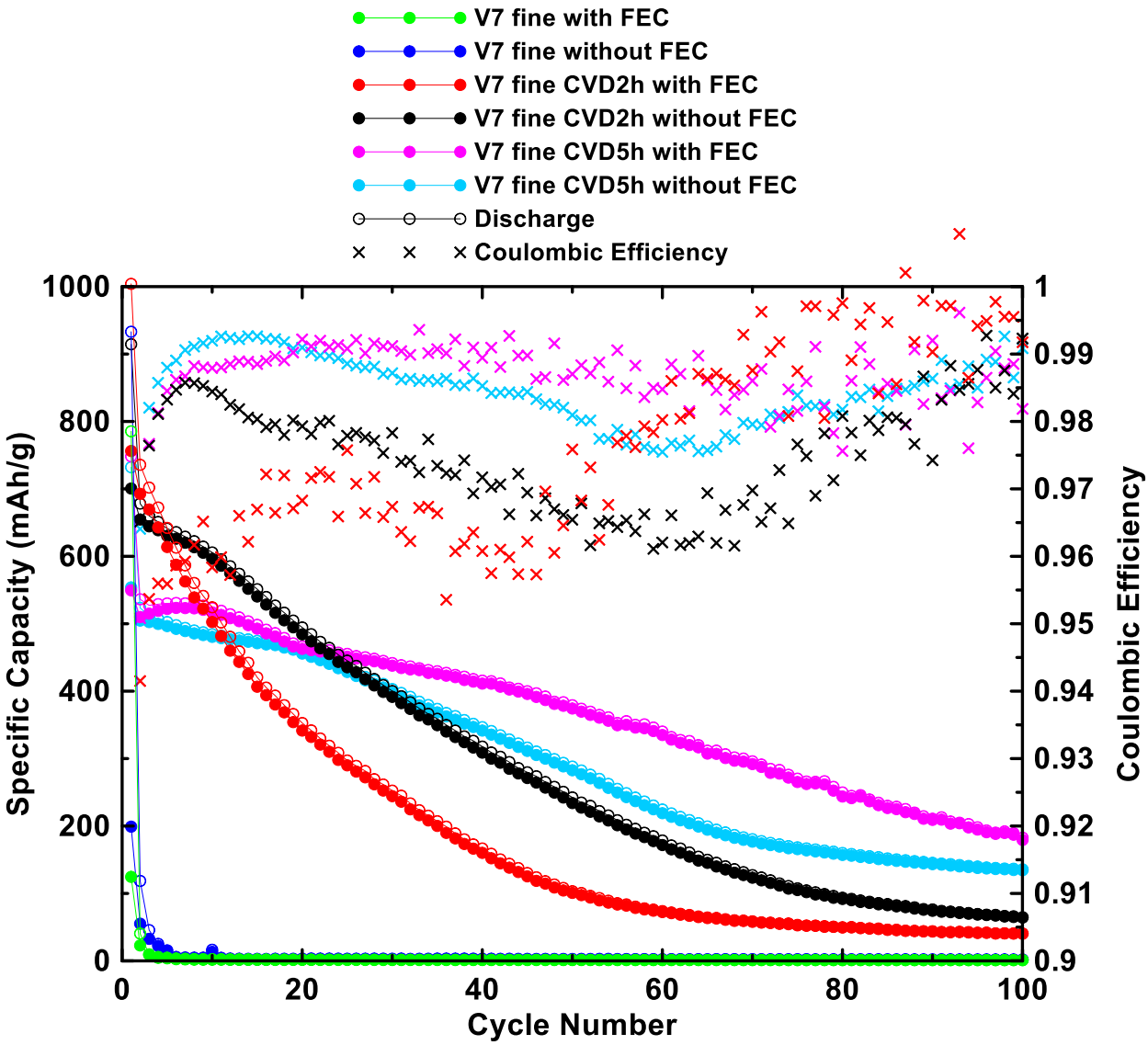

Figure 5.2 Cycling performance of carbon coated and uncoated 3M-V7 powder.

5.3 Synthesis of nano Si/Carbon Composites in an Opposing Screw CVD Reactor

5.3.1 Introduction

As shown in the previous section, it was found that the fine Si-alloy particles would aggregate in the opposing screw CVD reactor. The result was interesting enough to try more fine powders. This section will describe the result of processing nano-Si (n-

Si) powder in the new CVD reactor and the electrochemical performance of the resulting product in lithium-ion batteries.

5.3.2 Experimental

The experimental conditions in the preparation of C-(n-Si) composite particles were essentially the same as that described in Section 5.1.2. The only differences are that the CVD processing times were shorter (e.g. 1 hour and 2 hours) and instead of 3M V7 alloy powder, n-Si powder (Hongwu New Material, particle size: 30-50 nm) was used. Composite samples are identified here as C-nSi(xh), where x is the number of hours processing time in the CVD reactor.

5.3.3 Results and Discussion

A SEM image of uncoated n-Si powder is shown in Figure 5.3(a). It is a very fine powder having an average particle size of about 50 nm. After 1 hour of carbon coating procedure the C-nSi(1h) sample was formed. In this sample, the nano Si powder aggregated into much bigger (~30 μm) secondary particles, as shown in Figure 5.3(b) and 5.3(c). The surface of these secondary particles is highly porous. The n-Si particles appear to have been coated and bonded together by the deposited carbon. After another hour of processing, the resulting C-nSi(2h) secondary particles did not get any bigger, but their surface appeared slightly smoother (Figure 5.3(d)). Figure 5.3(e) and 5.3(f) show SEM images of the C-nSi(2h) sample's cross section. The sample has a sponge-like internal structure with high porosity. The white spots on the bottom of the particle in image (e) and (f) are likely an insulating silicon carbide formed by back-sputtering during the cross-sectioning process, which appears white due to charging in the SEM.

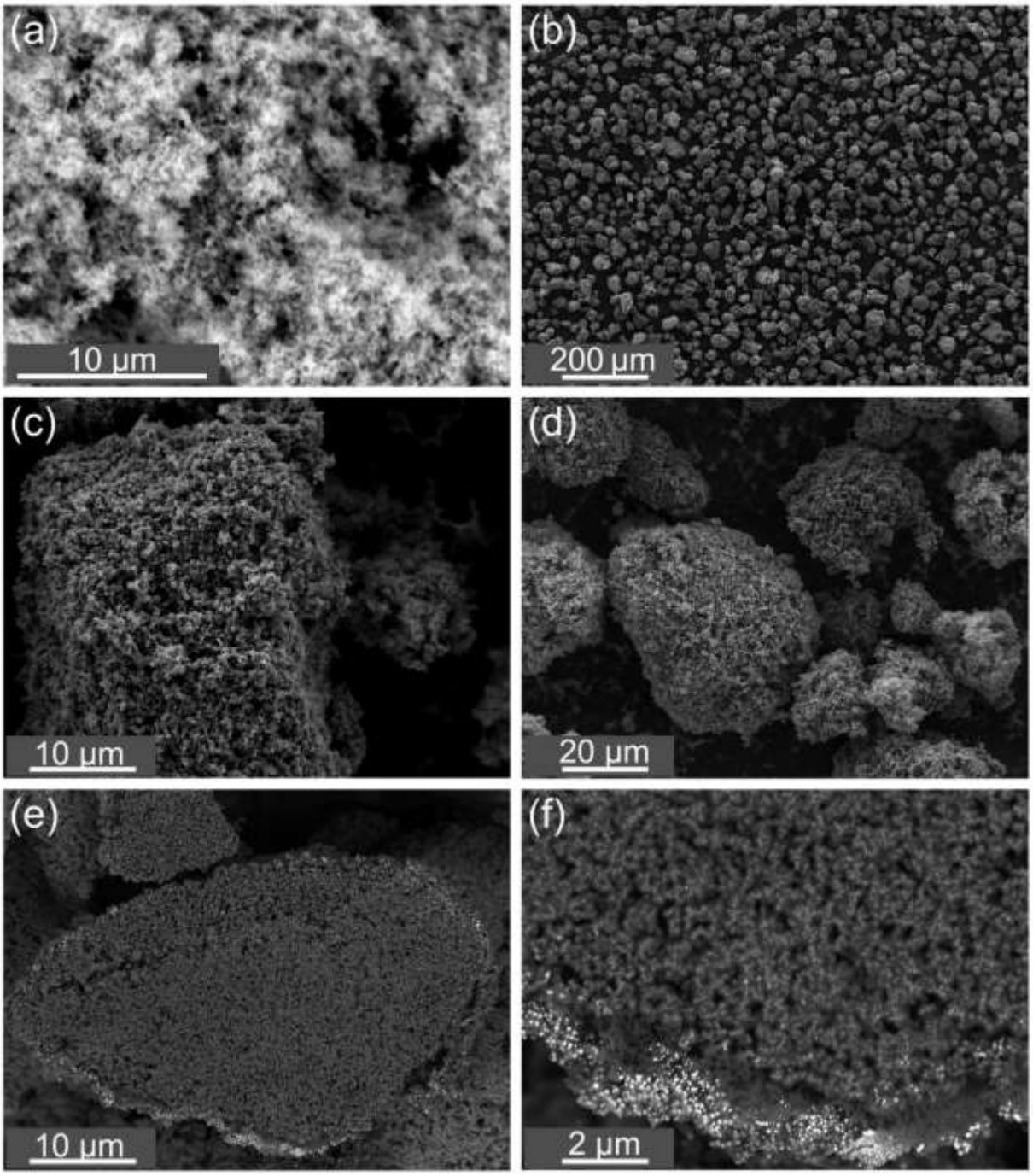

Figure 5.3 (a) SEM image of nano Si powder; (b), (c) SEM images of C-nSi(1h); (d), (e), (f) SEM image and cross-section of C-nSi(2h). Images (b-d) were taken with SE and (e,f) with BSE imaging mode.

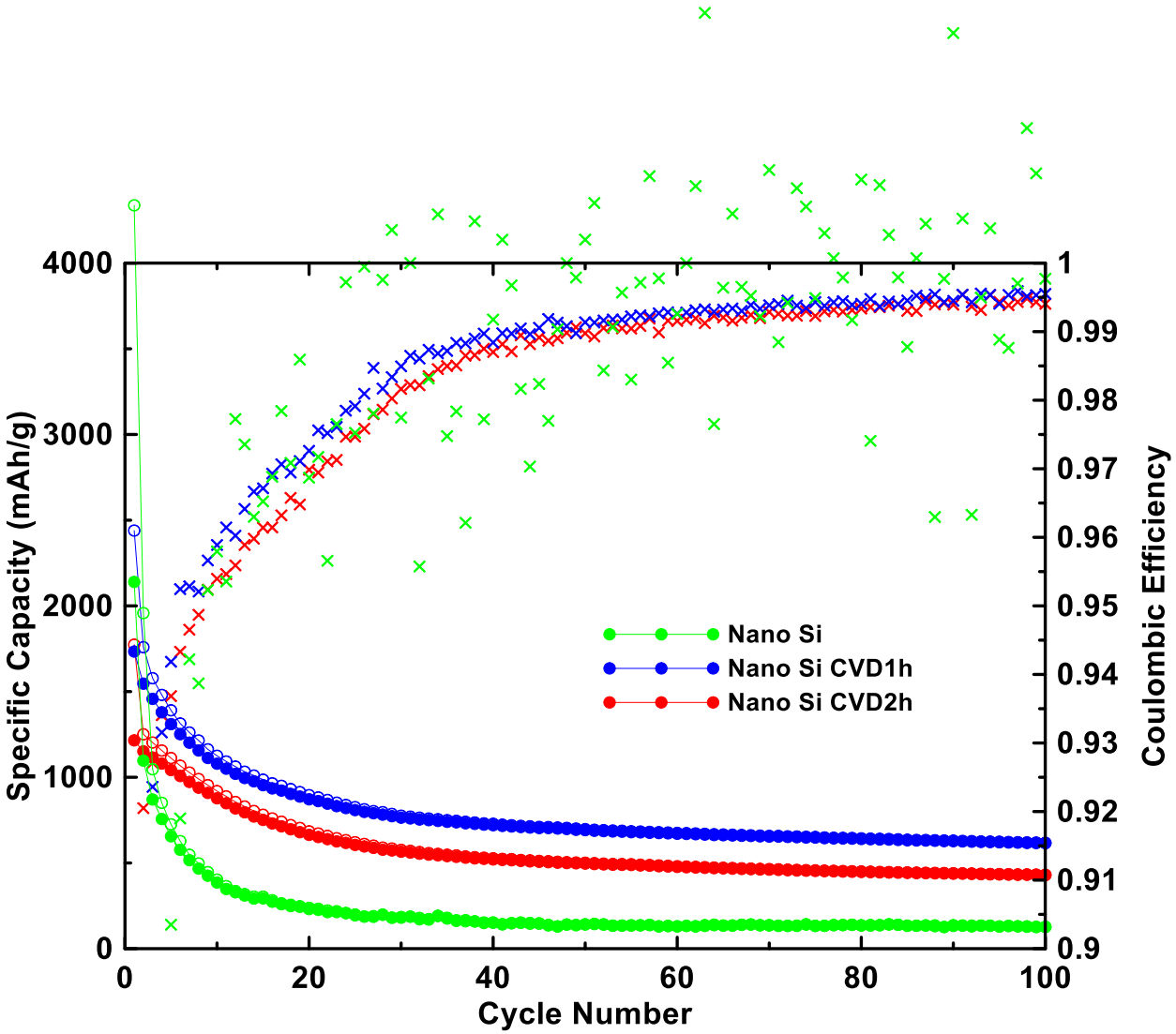

Figure 5.4 Cycling performance of carbon coated and uncoated nano Si powder.

Figure 5.4 shows the cycling performance of nSi compared to C-nSi(1h) and C-nSi(2h) in lithium cells. The nSi fades rapidly, while the coated samples have significant improvement. The coated samples also have much lower irreversible capacity. Further improvements are possible if the coating time increases or changing to bigger particle size of nSi.

5.4 Synthesis of nSi /Carbon Composites by Mechanofusion

5.4.1 Introduction

Graphite can maintain a stable structure during the charging and discharging process of the battery, while silicon has a much larger capacity, but suffers from large volume expansion and particle fracture. It has been found that fracture does not occur for Si nanoparticles less than 150 nm in diameter.[47] However, even without particle fracture, the large volume expansion of n-Si disrupts the SEI layer, resulting in continuous SEI formation. n-Si volume expansion/contraction during cycling can also lead to electrical disconnection of the particles. Both SEI formation and electrical disconnection of active particles leads to capacity fade. For n-Si to be utilized good electrical connection needs to be maintained. One strategy of accomplishing this is by making graphite/n-Si composites. Therefore, mixing and dispersing nano silicon particles onto flake graphite by mechanofusion was tried as a method for making such composite materials. The resulting composites were then carbon coated to protect the n-Si from exposure to electrolyte. The microstructure of the resulting particles was very interesting, and the composite particles exhibited good cycling characteristics in Li cells. This section will describe some examples of graphite/n-Si composite particles produced by mechanofusion and CVD.

5.4.2 Experimental

20 g of commercial KS6L graphite powder (from C-Nergy) and 2 g of n-Si powder (Hongwu New Material, particle size: 30-50 nm) were placed in the chamber of a Hosokawa AM-15F mechanofusion system. The press-head gap was 1 mm, and the scraper gap was 0.4 mm. The rotation speed was around 1500 rpm. Samples were taken after the mechanofusion processing for different time periods. The processing also

repeated for different additives (propylene glycol (Sigma Aldrich >99.5%), PVDF (Kynar HSV 900; 1% and 5% with propylene glycol solvent), and PVDF (5% with NMP solvent (NMP, Sigma Aldrich, anhydrous 99.5%)). Finally, the sample with 5% of PVDF (NMP solvent) was carbon coated by CVD for different times, using the same procedure in described in Section 5.1.2. Sample powder morphologies were studied by SEM (TESCAN MIRA 3 LMU variable pressure Schottky field SEM) at 5.0 kV and 20.0 kV.

For samples shown in Figure 5.6 and 5.8, electrode slurries were prepared from the samples, carbon black (Super C65, Imerys Graphite and Carbon), and lithium polyacrylate (LiPAA) (from a 10 weight% LiPAA aqueous solution, made by neutralizing a polyacrylic acid solution (Sigma-Aldrich, average molecular weight of 250000 g per mol, 35 wt% in water) with LiOH·H2O (Sigma Aldrich, 98%)) in a mass ratio of 80/10/10. For the rest of the samples (shown in Figure 5.10) with or without carbon coating, the electrode slurries were prepared by same carbon black and LiPAA but in a volumetric ratio of 70/5/25 (corresponding to a 83/4/13 weight ratio). Slurries were mixed using a high-shear mixer equipped with a Cowles blade at 5000 rpm for 10 min. and then spread onto electrolytic copper foil (Furukawa Electric, Japan) with a 0.1 mm gap coating bar. The coatings were dried in air at 120 °C for 40 min., punched into 1.3 cm (in diameter) disks, and then heated under vacuum for a few hours at 120 °C with no further air exposure before cell assembly.

Electrodes were assembled into 2325-type coin cells with a lithium foil (Aldrich, 99.9%) counter/reference electrode separated by two layers of separators (Celgard 2300) in an Argon filled glove box. 168 μL of electrolyte was used in each half cell. The electrolyte consisted of 1M $LiPF_6$ (BASF) in a solution of ethylene carbonate (EC),

diethyl carbonate (DEC), and with mono-fluoroethylene carbonate additive (FEC) (volume ratio 3:6:1, all from BASF). Cells were cycled at 30 °C between 7 mV and 0.9 V using a Neware battery testing system at a C/10 rate for the 1st cycle and a C/5 rate for the following cycles. Cells were held at 7 mV after discharge (lithiation) until their rate decreased to C/20 for the first cycle or C/10 for subsequent cycles, to simulate CCCV charging in a full cell.

5.4.3 Results and Discussion

Figure 5.5(a) shows an SEM image of KS6L graphite powder. It consists of flake graphite particles with an average size of about 5 μm. Figure 5.5(b) shows an SEM image of n-Si powder. It consists of very fine powder having an average particle size of about 50 nm. The n-Si and graphite powder were ground together using a mortar and pestle for 10 minutes. An SEM image of the resulting sample is shown in Figure 5.5(c). In this sample, the dispersion of nano Si was not good, the fine Si powder mostly being present in ~10 μm agglomerates. Figure 5.5(d-f) show SEM images of mechanofusion processed samples after 5, 10, and 20 minutes processing time. These samples all showed improved dispersion of nano Si on the surface of flake KS6l graphite. Most of the nSi was still present as aggregates, however the aggregate size was reduced greatly from the 10 μm size for the hand mixed samples to a size of about 3 μm for the mechanofusion made samples. For the mechanofusion samples it was found that the processing time did not affect the dispersion quality after 5 min. Figure 5.6 shows the cycling performance of all the KS6L-nSi samples. All three mechanofusion samples have similar capacities and they are higher than the hand mixed sample. The hand mixed sample also suffers from a

greater capacity fade rate. It is believed that the improved performance of the mechanofusion made samples are a result of the better dispersion of Si in the sample.

In order to investigate if further improvements could be made to the nSi dispersion, different polymer and solvent combinations were added to try to reduce the tendance of nSi particles to aggregate. Some of the best result samples are discussed below.

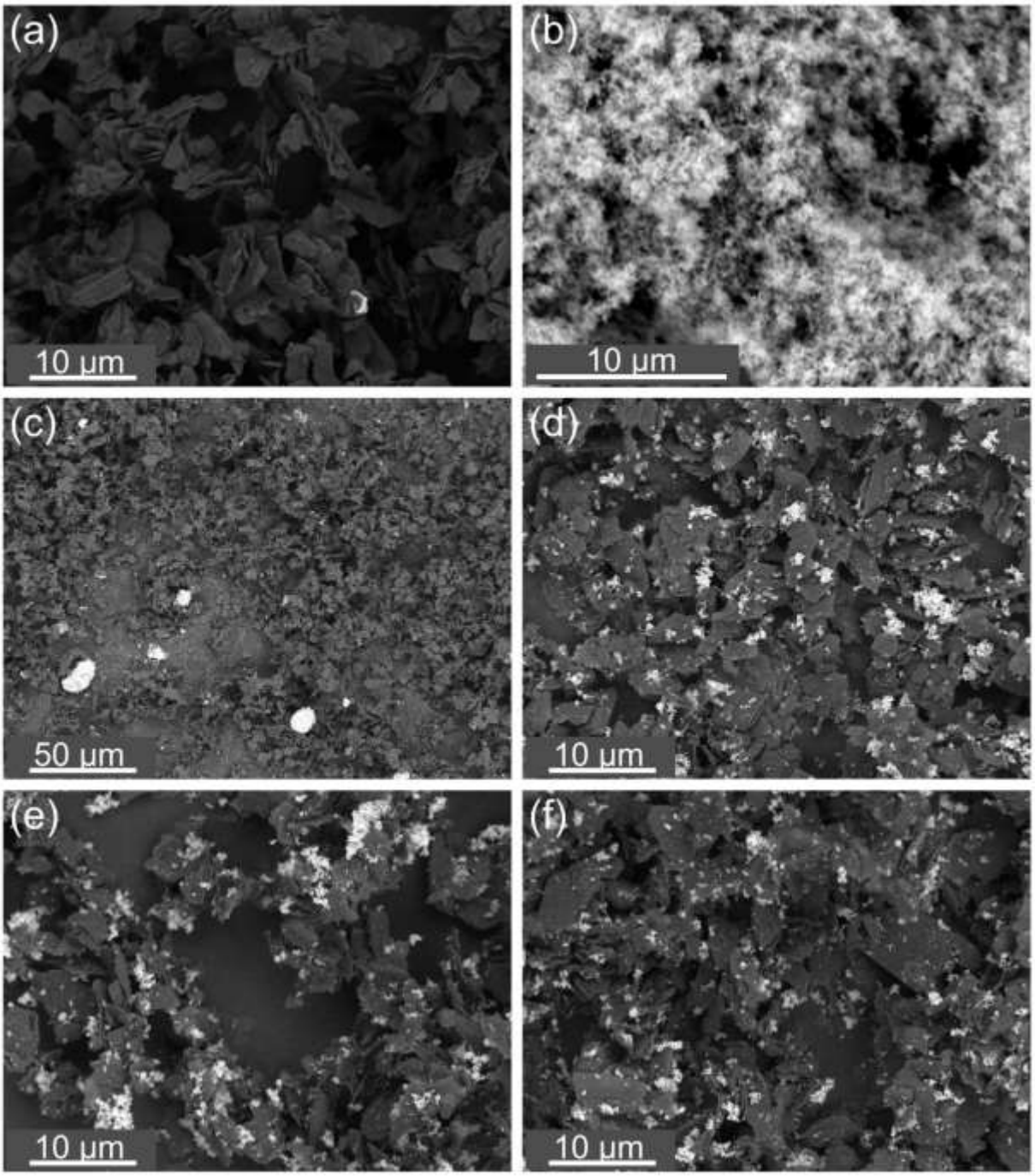

Figure 5.5 (a) SEM image of KS6L graphite powder; (b) SEM image of nano Si powder; (c) SEM image of KS6L-nSi mixture made by hand blending for 10 min; (d), (e), (f) SEM images of KS6L-nSi mixture made by mechanofusion processing for 5, 10, 20 min.

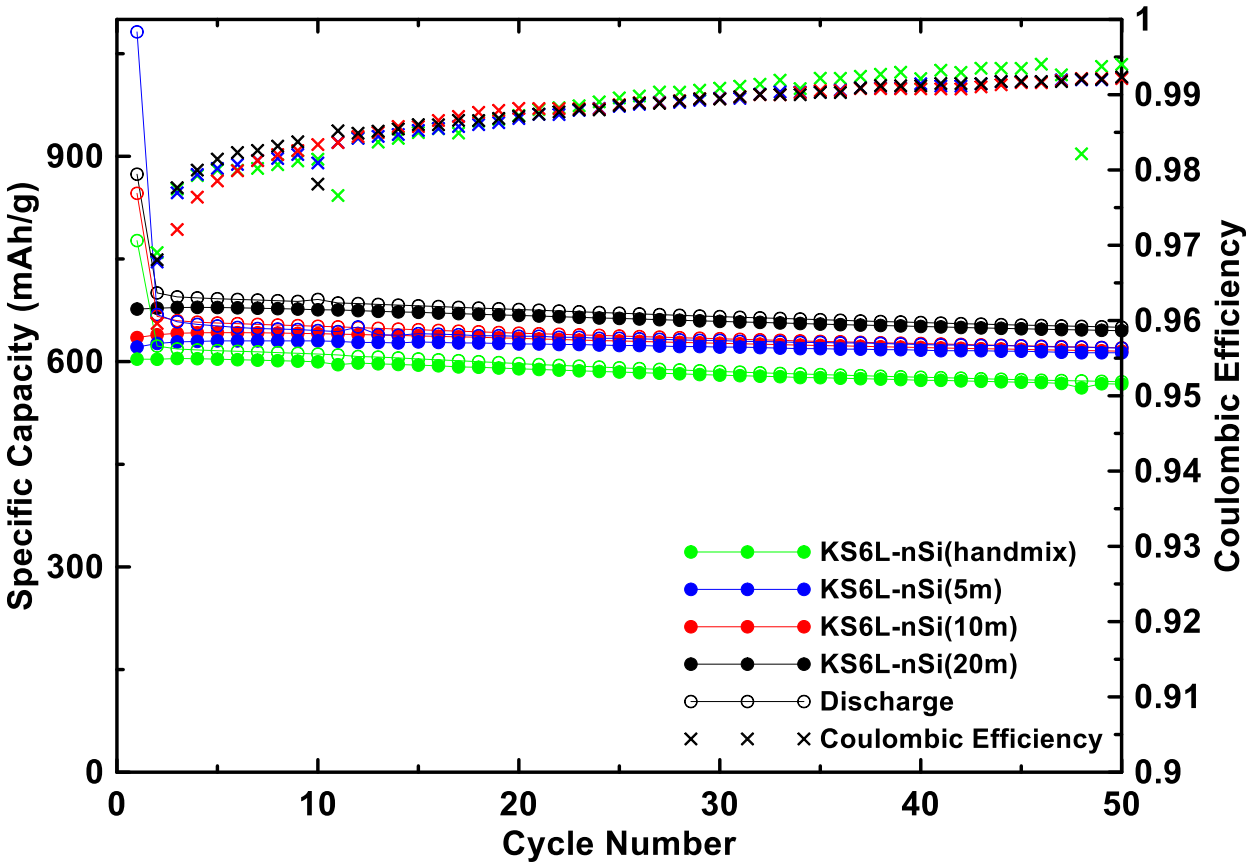

Figure 5.6 Cycling performance of KS6L-nSi mixtures by hand mix and mechanofusion machine.

Figure 5.7(a) shows an SEM image of KS6L-nSi powder mechanofusion processed with PG (0.3 mass ratio of total sample weight) for 15 min. Compared to the mechanofusion processed samples with no PG (Figure 5.5(d-f)), the sample with PG shows some more finely dispersed Si, however large aggregates are still present. Figure 5.7(b) shows an SEM image of KS6L-nSi powder mechanofusion processed with a PVDF PG solution for 10 min. The mass ratio of KS6L, nSi, PVDF was 10:1:0.1. This sample has the best dispersion overall, with most of the nSi being present either as single nanoparticles or submicron aggregates. Figure 5.7(c) shows an SEM image of KS6L-nSi powder mechanofusion processed with PVDF PG solution for 10 min, but with a KS6L,

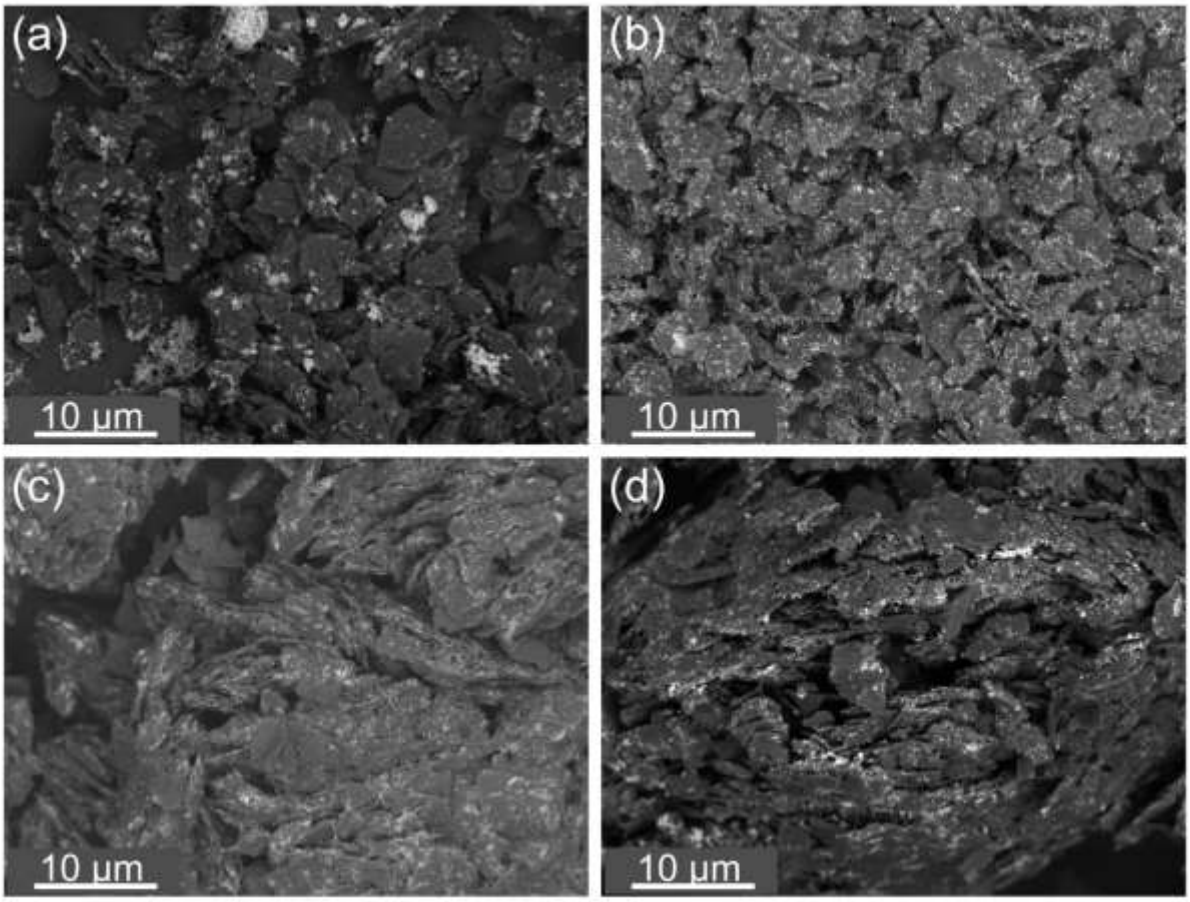

Figure 5.7 (a) SEM image of KS6L-nSi (10:1)(PG, 15m) powder; (b) SEM image of KS6L-nSi-PVDF (10:1:0.1)(PG, 10m) powder; (c) SEM image of KS6L-nSi-PVDF (10:1:0.5)(PG, 10m) powder; (d) SEM image of KS6L-nSi-PVDF (10:1:0.5)(NMP, 10m) powder.

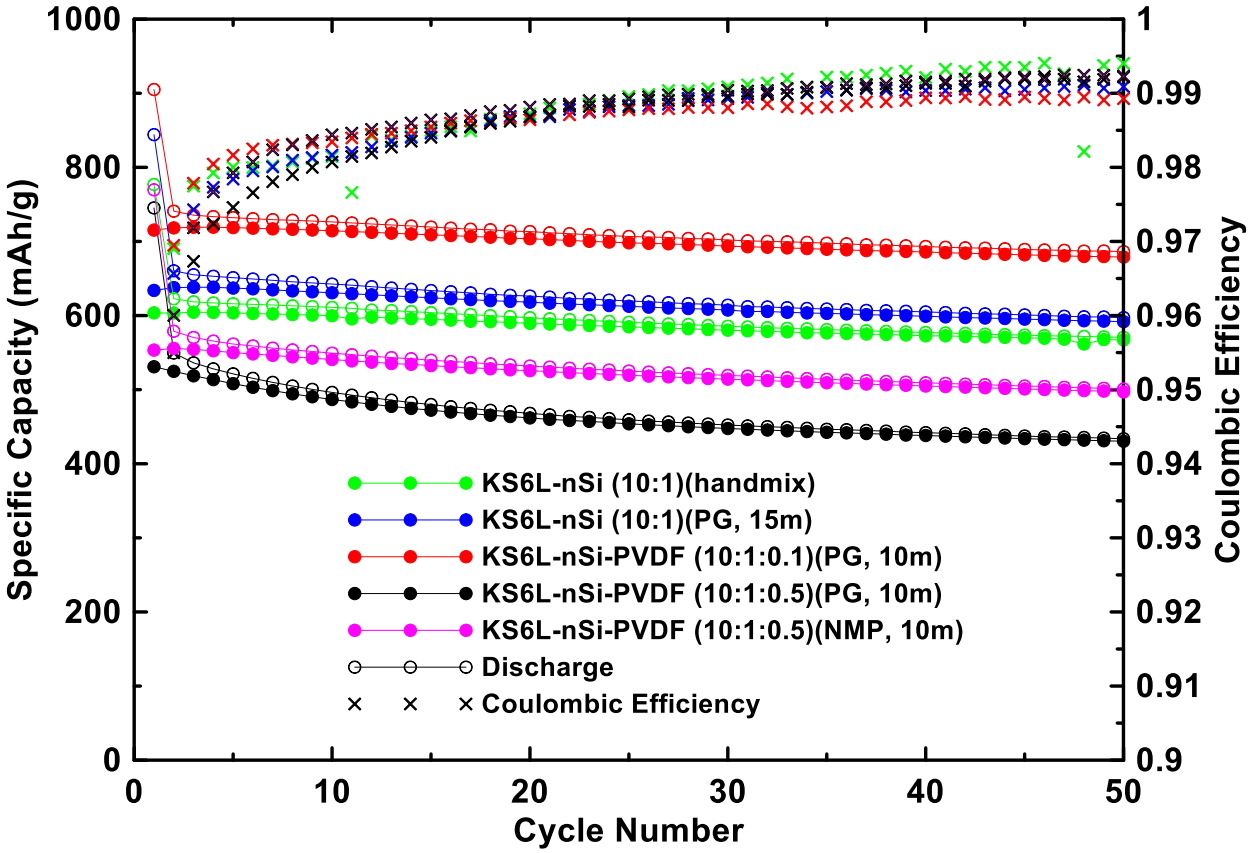

Figure 5.8 Cycling performance of KS6L-nSi mixtures of different binder combinations.

nSi, PVDF the mass ratio of 10:1:0.5. With five times more of PVDF binder in the sample, the nSi dispersion of this sample is much like the sample shown in Figure 5.7(b). However, due to the high content of PVDF binder, the KS6L, nSi, PVDF 10:1:0.5 sample tends to form compact KS6L-nSi secondary particles with various size ranges. Figure 5.7(d) shows an SEM image of KS6L-nSi powder mechanofusion processed with PVDF NMP solution for 10 min, the mass ratio of KS6L, nSi, PVDF for this sample being 10:1:0.5. In this sample, the graphite flakes are most tightly bonded to each other. The cycling performance of all KS6L-nSi+additive samples is shown in Figure 5.8. The capacity fade rate was not improved compared to the baseline for any of the samples. In

fact the (10:1:0.5)(PG, 10m) had a greater capacity fade than the baseline. This sample also had the lowest reversible capacity and the highest irreversible capacity. This suggests that there is poor electrical connection to the Si in the sample, with much of the Si being electrically disconnected initially, resulting in low capacity, and additional Si becoming disconnected as cycling progresses, resulting in high irreversible capacity and capacity fade. An increase in reversible capacity, a reduction in irreversible capacity and improved capacity retention results when the amount of PVDF is reduced to the (10:1:0.1)(PG, 10m) sample. This electrode had the best performance, having a much higher capacity and lower irreversible capacity than the baseline hand mixed sample with no additives. This suggests that excessive amounts of insulating PVDF may result in poor electrical connection to the Si particles. However, removing PVDF completely (the (10:1)(PG, 15m) sample) results in a significant reduction in reversible capacity and an increase in irreversible capacity. Therefore, the inclusion of some PVDF in the KS6L-nSi composite is beneficial.

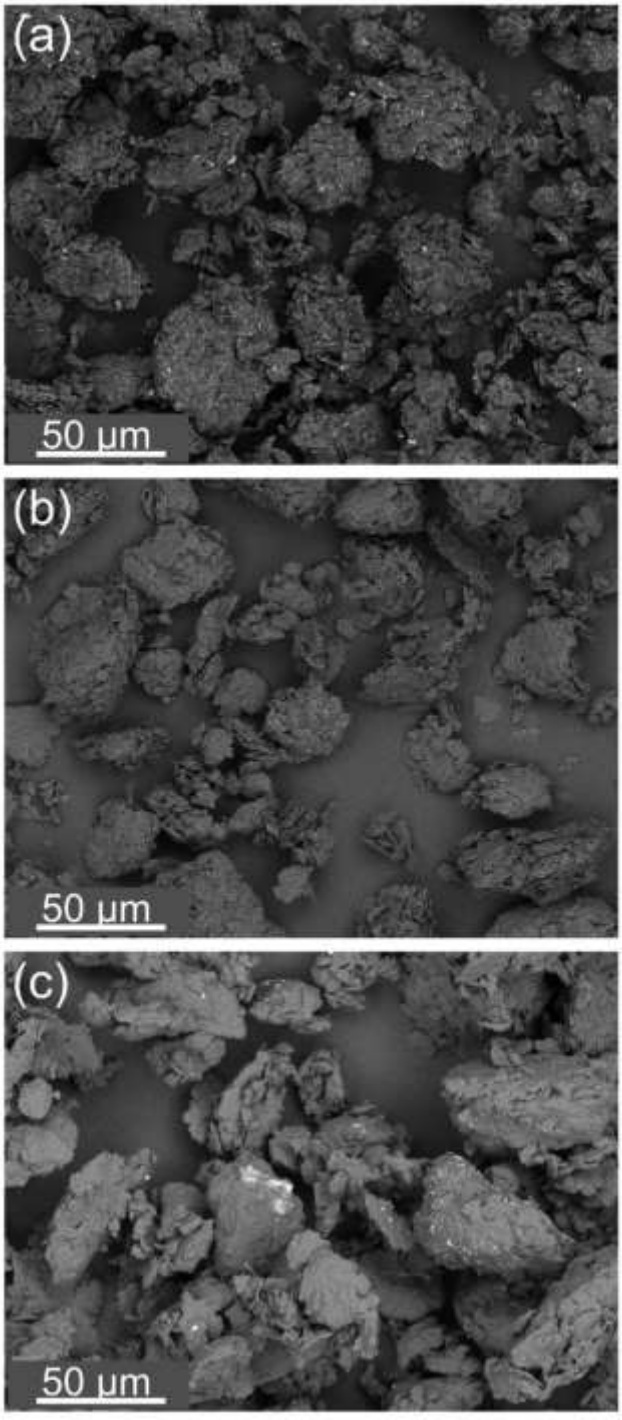

Figure 5.9 (a) SEM image of KS6L-nSi-PVDF(NMP) (10:1:0.5, uncoated) powder; (b) SEM image of KS6L-nSi-PVDF(NMP) (10:1:0.5, CVD2.5h) powder; (c) SEM image of KS6L-nSi-PVDF(NMP) (10:1:0.5, CVD6h) powder.

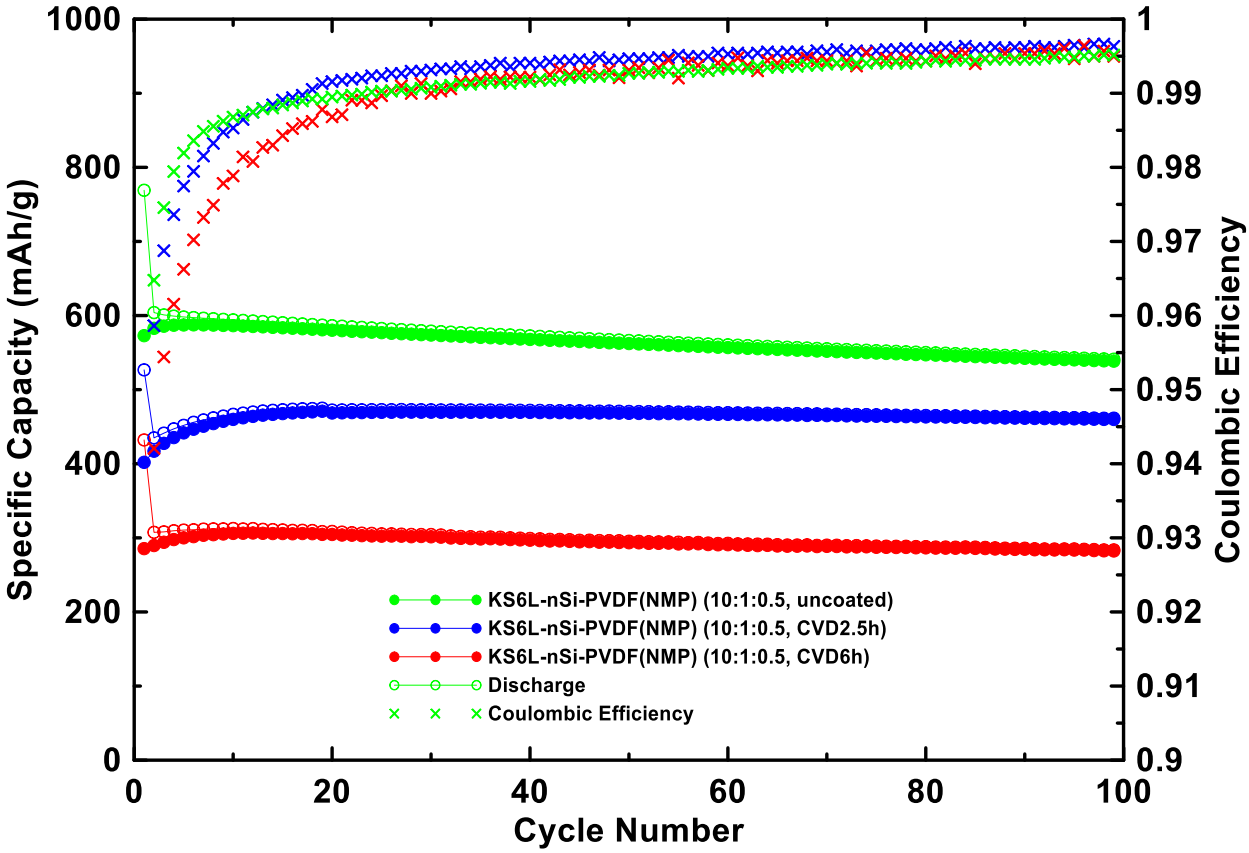

Figure 5.10 Cycling performance of KS6L-nSi-PVDF(NMP) uncoated and coated mixtures.

Also shown in Figure 5.8, the (10:1:0.5)(NMP, 10m) sample had lower reversible capacity and higher irreversible capacity than the (10:1) hand mixed baseline. Nevertheless, this sample had the most compact secondary particles. Therefore, it was thought that this sample could be most amenable towards CVD coating and this sample was chosen to be coated with the CVD reactor. The results are below.

Figure 5.9(a) shows an SEM image of uncoated KS6L-nSi-PVDF(NMP) powder. In this BSE image, the contrast between elements Si and C is high. Lots of fine secondary particles are present. After this sample was carbon coated in the CVD reactor for 2.5 hour, the contrast between element Si and C became low as shown in Figure 5.9(b), this

indicates that the particles are covered by a layer of amorphous carbon. However, there are still some fine particles in the coated sample. Figure 5.9(c) shows the sample after 6 hours of CVD processing. The fine Si particles now in general cannot be seen in the BSE image. The white spots showed in Figure 5.9(c) are believed to be impurities, since they are generally larger than the Si particles and are highly insulating (as evidenced by their being bright white, due to charging in the SEM). This needs confirmation by EDS. The source of these impurities is unknown. The SEM results suggest that there was aggregation of fine secondary particles during the mechanofusion process. The cycling performance of the uncoated and carbon coated (10:1:0.5) samples is shown in Figure 5.10. There are significant differences in the capacity of these materials. The uncoated sample has biggest specific capacity, but it has the most capacity fade overall. The carbon coated samples capacity initially increases for the first 10-15 cycles. It is not known why this occurs. Subsequent to this initial capacity increase, these samples have very little capacity fade, although their specific capacities are much lower than the uncoated sample. The 2.5h CVD coated sample had the highest capacity and the least capacity fade of the coated samples. Increasing the carbon coating thickness (in the 6h CVD sample) resulted in a lower capacity, due to the high carbon content and an increase in fade rate. The 2.5h CVD coated sample is a highly attractive material, having almost no fade and a specific capacity of about 480 mAh/g, which represents a 30% improvement in specific capacity compared to a conventional graphite electrode. This sample should be investigated further.

CHAPTER 6 CONCLUSIONS AND FUTURE WORK

6.1 Conclusions

In this work, methods for the chemical vapor deposition (CVD) of carbon and the hydrothermal deposition of carbon were evaluated for carbon coating lithium-ion battery active material powders. The unique methods developed were found to be useful in making lithium-ion battery material composites with unique morphologies.

To coat powders by CVD at the laboratory scale, a laboratory CVD furnace with an opposing screw fluidized bed reactor was developed that concentrate and fluidize powders, so that they can be efficiently coated by CVD at the laboratory scale. This reactor was constructed out of common laboratory equipment. The properties of the carbon coating deposited by the opposing screw CVD reactor were carefully studied by depositing carbon onto alumina powder, which is inactive lithium-ion cells. The deposited carbon layer by this method had a density of 1.84 g/mL and a capacity of 225 mAh/g when cycled between 0.007 V and 0.9 V in lithium-ion half cells. The carbon coating was evaluated as a means to extend the cycle life of powdered graphite active material. The deposited carbon resulted in a significant reduction in the graphite surface area, as it closes the pores of the graphite particles. Carbon coating was also found to be effective in improving capacity retention and reducing polarization growth during the cycling of graphite electrodes.

In Chapter 4, a hydrothermal method was utilized as another method to apply carbon coatings to Li-ion battery negative electrode materials. The applied coatings were highly uniform and were slightly denser (1.89 g/mL) compared to carbon coatings made by the CVD method (1.84 g/mL). The surface area of the hydrothermally deposited

carbon was hundreds of times larger compared to carbon coatings made by the CVD method. This is likely due to gas release during the carbonization process at 800 °C. Nevertheless, the reversible capacity of hydrothermally deposited carbon is similar (230 mAh/g when cycled between 0.007 V and 0.9 V in lithium-ion half cells) to that of CVD deposited carbon and the hydrothermally deposited carbon layer is effective in improving graphite cycle life.

It was found that the newly developed opposing screw CVD reactor and the mechanofusion method enable the synthesis of unique composite particles that have interesting properties as lithium-ion battery negative electrode materials. These methods and the new materials they enable provide substantial opportunities for future work.

6.2 Future work

The lab-scale carbon coating methods developed in this thesis enable laboratory developed experimental materials to be carbon coated. In this way performance can be improved and the way active materials would be utilized commercially can be more realistically represented. These methods will therefore be important for the development of new Li-ion battery materials in the laboratory. For example, although not shown in this thesis, many more negative electrode active materials (e.g. crystalline-Si, Si-Cr alloys, SiOx, alloy-graphite composites) were carbon coated using the opposing screw CVD reactor and hydrothermal methods. All these materials showed some level of cycle life improvement from the carbon coating, demonstrating the near universal applicability of these methods. Also, this new CVD reactor might have ability to other non-battery applications too. Being miniaturized, the CVD reactor not only has the same basic functions to cover various coating tasks as any other large commercial device does, but

also can better handle small samples. This device can be very handy in situations where multiple small samples with different physical properties need to be processed quickly. It can save the operator a lot of time due to its adjustment-free nature and the ability to quickly change the core reaction tube. For carbon coating, it can make non-conductive small samples conductive to avoid electrostatic charging effects in some applications or to encapsulate samples to eliminate evaporation. Also, this reactor can be used on other coatings too, by using different reactive gases, one can form nitride or carbonitride coating or even metal coatings onto small powder samples, for example, Sanjurjo et al. deposited Ti, TiN and TiOx on copper in a fluidized bed reactor to get copper particles better oxidation, corrosion and corrosion resistance,[48] their process involved a complicated vertical CVD furnace with fluidizing gas to maintain the precursor particles fluidized.[49] It is possible to use the simple opposing screw CVD reactor to do the same job and it might be better, since this reactor is especially good for dealing with denser precursor powders, like copper. Using this lab-scale broad adaptability reactor is a low cost and effective solution for those who need to process many small samples quickly. There is lots of work that could be done with this little machine.

It was observed that the opposing screw CVD reactor can synthesize unique composite materials from fine particle feedstocks. In this apparatus, fine submicron powders are simultaneously carbon coated and aggregated together to form much bigger particles (> 10 μm), which are themselves carbon coated on their surface. The resulting particles are composed internally of the fine particle feedstock and porosity with an outer carbon shell. This structure could be very useful for high volume change silicon-based materials where the porosity can accommodate the Si volume expansion, while the outer

carbon shell could protect the Si from electrolyte. The exploring work in Chatper 5 didn't end yet, there are still lot of room to improve, one can try to work Si into flake graphite and then use CVD reactor to protect the composite particles. One can try to use the CVD reactor to spheroidize irregular shaped fine particles by applying thick coating and the aggregating effect to reduce surface area of materials with complex structures. This might be a way to improve the electrochemical performance of Si based anode materials, especially for silicon materials with structure-dependent properties. For example, Chan et al. showed that silicon nanowires achieved almost the theoretical capacity for silicon anodes,[50] however, the practical capacity fades significantly during cycling. This is because of material that becomes electrically disconnected during cycling. An appropriate treatment from the opposing screw CVD reactor could be of benefit in this application. A coating of carbon applied by a CVD reactor could significantly reduce the Si nanowire surface area by binding the nanowires together and aggregating them into bigger spherical balls. The carbon deposited between and around the Si nanowires could provide much better electrical connection and structural support.

The CVD furnace also decorated the surface of materials with lots of carbon fibers when the coated material included transition metals in its composition. The carbon fibers can be useful to increase the electrode mechanical strength and to adhesive stronger with current collector. They can also improve electrical conductivity of the coating. This can improve rate capability and cycle life, especially for Si-based materials that suffer from volume change. Si alloys can be well coated in the newly developed CVD reactor. Additionally, carbon fibers may be deposited on surfaces if transition metals are present, which can improve electrical conductivity. This may not only have

applications for Li-ion battery materials, but might also be good for other applications.eg. adsorbent material or slow-release drugs.

It was found that the CVD method provided a denser carbon coating, but it was difficult to apply uniformly, especially for compositions containing transition metals. The hydrothermal method resulted in much more uniform carbon coatings, however the coated carbon was highly porous and it was also found that the coated particles by hydrothermal method tend to be fused together during the carbonization process (800 °C). It would be interesting to combine the methods described here to realize the benefits of both methods: for instance, using the opposing screw CVD reactor to carbonize hydrothermally carbon coated particles, and even applying a second carbon coating by CVD over the porous hydrothermally coated carbon layer. This could provide a uniform and dense carbon coating. Combining the two carbon coating methods could result in the formation of more diverse carbon layers, which may be highly attractive and should be studied.

REFERENCES

1. Nitta, N., Wu, F., Lee, J. T., & Yushin, G. (2015). Li-ion battery materials: present and future. Materials today, 18(5), 252-264.

2. Ellis, B. L., Town, K., & Nazar, L. F. (2012). New composite materials for lithium-ion batteries. Electrochimica Acta, 84, 145-154.

3. Obrovac, M. N., & Christensen, L. (2004). Structural changes in silicon anodes during lithium insertion/extraction. Electrochemical and solid-state letters, 7(5), A93.

4. Feng, Z. Y., Peng, W. J., Wang, Z. X., Guo, H. J., Li, X. H., Yan, G. C., & Wang, J. X. (2021). Review of silicon-based alloys for lithium-ion battery anodes. International Journal of Minerals, Metallurgy and Materials, 28(10), 1549-1564.

5. Kasavajjula, U., Wang, C., & Appleby, A. J. (2007). Nano-and bulk-silicon-based insertion anodes for lithium-ion secondary cells. Journal of power sources, 163(2), 1003-1039.

6. Takami, N., Inagaki, H., Tatebayashi, Y., Saruwatari, H., Honda, K., & Egusa, S. (2013). High-power and long-life lithium-ion batteries using lithium titanium oxide anode for automotive and stationary power applications. Journal of power sources, 244, 469-475.

7. Asenbauer, J., Eisenmann, T., Kuenzel, M., Kazzazi, A., Chen, Z., & Bresser, D. (2020). The success story of graphite as a lithium-ion anode material–fundamentals, remaining challenges, and recent developments including silicon (oxide) composites. Sustainable Energy & Fuels, 4(11), 5387-5416.

8. Mao, C., Wood, M., David, L., An, S. J., Sheng, Y., Du, Z., ... & Wood, D. L. (2018). Selecting the best graphite for long-life, high-energy Li-ion batteries. Journal of The Electrochemical Society, 165(9), A1837.

9. Yazami, R., Zaghib, K., & Deschamps, M. (1994). Carbon fibres and natural graphite as negative electrodes for lithium ion-type batteries. Journal of power sources, 52(1), 55-59.

10. Safran, S. A. (1980). Phase diagrams for staged intercalation compounds. Physical Review Letters, 44(14), 937.

11. Zheng, T., Reimers, J. N., & Dahn, J. R. (1995). Effect of turbostratic disorder in graphitic carbon hosts on the intercalation of lithium. Physical Review B, 51(2), 734.

12. Kim, J., Yun, A. J., Sheem, K. Y., & Park, B. (2021). Identifying the Association between Surface Heterogeneity and Electrochemical Properties in Graphite. Nanomaterials, 11(7), 1813.

13. Attia, P. M., Chueh, W. C., & Harris, S. J. (2020). Revisiting the t0. 5 dependence of SEI growth. Journal of the Electrochemical Society, 167(9), 090535.

14. Zheng, Z., Zhang, J., & Huang, J. Y. (1996). Observations of microstructure and reflectivity of coal graphites for two locations in China. International journal of coal geology, 30(4), 277-284.

15. Li, H., Feng, Q., Ou, L., Long, S., Cui, M., & Weng, X. (2013). Study on washability of microcrystal graphite using float–sink tests. International Journal of Mining Science and Technology, 23(6), 855-861.

16. Hantel, M. M., Kaspar, T., Nesper, R., Wokaun, A., & Kötz, R. (2011). Partially reduced graphite oxide for supercapacitor electrodes: Effect of graphene layer spacing and huge specific capacitance. Electrochemistry Communications, 13(1), 90-92.

17. Li, H., & Zhou, H. (2012). Enhancing the performances of Li-ion batteries by carbon-coating: present and future. Chemical Communications, 48(9), 1201-1217.

18. Elton, L. R. B., & Jackson, D. F. (1966). X-ray diffraction and the Bragg law. American Journal of Physics, 34(11), 1036-1038.

19. Patterson, A. L. (1939). The Scherrer formula for X-ray particle size determination. Physical review, 56(10), 978.

20. Pennycook, S. J., & Nellist, P. D. (Eds.). (2011). Scanning transmission electron microscopy: imaging and analysis. Springer Science & Business Media.

21. Larkin, P. (2017). Infrared and Raman spectroscopy: principles and spectral interpretation. Elsevier. P 2.

22. Tallant, D. R., Friedmann, T. A., Missert, N. A., Siegal, M. P., & Sullivan, J. P. (1997). Raman spectroscopy of amorphous carbon. MRS Online Proceedings Library (OPL), 498.

23. Schwan, J., Ulrich, S., Batori, V., Ehrhardt, H., & Silva, S. R. P. (1996). Raman spectroscopy on amorphous carbon films. Journal of Applied Physics, 80(1), 440-447.

24. Wang, Y., Alsmeyer, D. C., & McCreery, R. L. (1990). Raman spectroscopy of carbon materials: structural basis of observed spectra. Chemistry of Materials, 2(5), 557-563.

25. Tuinstra, F., & Koenig, J. L. (1970). Raman spectrum of graphite. The Journal of chemical physics, 53(3), 1126-1130.

26. Li, F., Tao, R., Cao, B., Yang, L., & Wang, Z. (2021). Manipulating the Light-Matter Interaction of PtS/MoS2 p–n Junctions for High Performance Broadband Photodetection. Advanced Functional Materials, 31(36), 2104367.

27. Luo, X., Peng, Z., Wang, Z., & Dong, M. (2021). Layer-by-Layer Growth of AA-Stacking MoS2 for Tunable Broadband Phototransistors. ACS Applied Materials & Interfaces, 13(49), 59154-59163.

28. Vahlas, C., Caussat, B., Serp, P., & Angelopoulos, G. N. (2006). Principles and applications of CVD powder technology. Materials Science and Engineering: R: Reports, 53(1-2), 1-72.

29. Goto, T., & Katsui, H, in Handbook of Solid State Chemistry, 1st ed., edited by R. Dronskowski, S. Kikkawa, and A. Stein (Wiley-VCH, Verlag, 2017), Vol. 2, pp. 399–428.

30. Ding, Y. S., Li, W. N., Iaconetti, S., Shen, X. F., DiCarlo, J., Galasso, F. S., & Suib, S. L. (2006). Characteristics of graphite anode modified by CVD carbon coating. Surface and Coatings Technology, 200(9), 3041-3048.

31. Suzuki, S., & Hibino, H. (2011). Characterization of doped single-wall carbon nanotubes by Raman spectroscopy. Carbon, 49(7), 2264-2272.

32. Talyzin, A., & Jansson, U. (1999). Preparation and characterization of C60S16 and C70S48 thin films. Thin Solid Films, 350(1-2), 113-118.

33. Cuesta, A., Dhamelincourt, P., Laureyns, J., Martinez-Alonso, A., & Tascón, J. D. (1994). Raman microprobe studies on carbon materials. Carbon, 32(8), 1523-1532.

34. Reich, S., & Thomsen, C. (2004). Raman spectroscopy of graphite. Philosophical Transactions of the Royal Society of London. Series A: Mathematical, Physical and Engineering Sciences, 362(1824), 2271-2288.

35. Dahn, J. R., Sleigh, A. K., Shi, H., Reimers, J. N., Zhong, Q., & Way, B. M. (1993). Dependence of the electrochemical intercalation of lithium in carbons on the crystal structure of the carbon. Electrochimica Acta, 38(9), 1179-1191.

36. Wang, C., Appleby, A. J., & Little, F. E. (2001). Electrochemical impedance study of initial lithium ion intercalation into graphite powders. Electrochimica acta, 46(12), 1793-1813.

37. Wang, H., & Yoshio, M. (2001). Carbon-coated natural graphite prepared by thermal vapor decomposition process, a candidate anode material for lithium-ion battery. Journal of power sources, 93(1-2), 123-129.

38. Ota, H., Sakata, Y., Inoue, A., & Yamaguchi, S. (2004). Analysis of vinylene carbonate derived SEI layers on graphite anode. Journal of the Electrochemical Society, 151(10), A1659.

39. Wang, J., & Obrovac, M. N. (2022). Lab-scale chemical vapor deposition onto powders. AIP Advances, 12(7), 075209.

40. Liu, L., Fan, Q., Sun, C., Gu, X., Li, H., Gao, F., ... & Dong, L. (2013). Synthesis of sandwich-like TiO2@ C composite hollow spheres with high rate capability and stability for lithium-ion batteries. Journal of Power Sources, 221, 141-148.

41. Zhang, W. M., Hu, J. S., Guo, Y. G., Zheng, S. F., Zhong, L. S., Song, W. G., & Wan, L. J. (2008). Tin-nanoparticles encapsulated in elastic hollow carbon spheres for high-performance anode material in lithium-Ion batteries. Advanced Materials, 20(6), 1160-1165.

42. Liu, H., Luo, S. H., Yan, S. X., Wang, Q., Hu, D. B., Wang, Y. L., ... & Yi, T. F. (2019). High-performance α-Fe2O3/C composite anodes for lithium-ion batteries synthesized by hydrothermal carbonization glucose method used pickled iron oxide red as raw material. Composites Part B: Engineering, 164, 576-582.

43. Poerschmann, J., Weiner, B., Koehler, R., & Kopinke, F. D. (2017). Hydrothermal Carbonization of Glucose, Fructose, and Xylose-Identification of Organic Products with Medium Molecular Masses. ACS Sustainable Chemistry & Engineering, 5(8), 6420-6428.

44. Zhou, Y. F., Xie, S., & Chen, C. H. (2005). Pyrolytic polyurea encapsulated natural graphite as anode material for lithium ion batteries. Electrochimica Acta, 50(24), 4728-4735.

45. Zheng, L., Wei, C., Garayt, M. D. L., MacInnis, J., & Obrovac, M. N. (2019). Spherically smooth cathode particles by mechanofusion processing. Journal of The Electrochemical Society, 166(13), A2924.

46. Zheng, L., Bennett, J. C., & Obrovac, M. N. (2020). All-dry synthesis of single crystal NMC cathode materials for Li-ion batteries. Journal of The Electrochemical Society, 167(13), 130536.

47. Liu, X. H., Zhong, L., Huang, S., Mao, S. X., Zhu, T., & Huang, J. Y. (2012). Size-dependent fracture of silicon nanoparticles during lithiation. ACS nano, 6(2), 1522-1531.

48. Sanjurjo, A., Wood, B. J., Lau, K. H., Tong, G. T., Choi, D. K., McKubre, M. C. H., ... & Church, N. (1991). Titanium-based coatings on copper by chemical vapor deposition in fluidized bed reactors. Surface and Coatings Technology, 49(1-3), 110-115.

49. Sanjurjo, A., McKubre, M. C. H., & Craig, G. D. (1989). Chemical vapor deposition coatings in fluidized bed reactors. Surface and coatings technology, 39, 691-700.

50. Chan, C. K., Peng, H., Liu, G., McIlwrath, K., Zhang, X. F., Huggins, R. A., & Cui, Y. (2008). High-performance lithium battery anodes using silicon nanowires. Nature nanotechnology, 3(1), 31-35.

APPENDIX: COPYRIGHT PERMISSION

The Chapter 3 is reproduced from [Wang, J., & Obrovac, M. N. (2022). Lab-scale chemical vapor deposition onto powders. AIP Advances, 12(7), 075209.], with the permission of AIP Publishing.